國立臺灣大學電機資訊學院光電工程學研究所

碩士論文

Graduate Institute of Photonics and Optoelectronics
College of Electrical Engineering and Computer Science
National Taiwan University

Master Thesis

奈米音波於砷化鎵奈米柱之波導模態

Nano-Acoustic Guided Waves in GaAs Nanorods

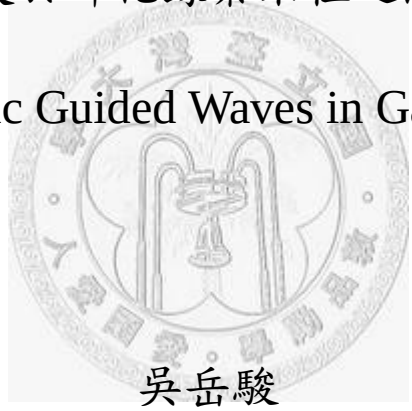

吳岳駿

Yueh-Chun Wu

指導教授：孫啟光 博士

Advisor: Chi-Kuang Sun, Ph.D.

中華民國 101 年 1 月

January, 2012

誌謝

在台大光電所待的兩年再多一點的日子裡，能夠完成一本碩士論文，首先得感謝我的指導教授，孫啟光老師。在奈米柱波導這個研究裡，總是被很多問題迷惑而使得自己停滯不前，在我已經不知道該怎麼辦的時候，若不是老師對我的耐心與包容，現在的我可能也還深陷在某個特定問題而無法自我放棄。老師的意見與建議總是能讓偏離軌道的我再走回來，在時間最急迫的時候，也還是願意花時間跟我討論，這個研究，如果不是老師的真知灼見，我可能還是迷惑在眾多實驗數據內而不知該如何解釋。每次的跟老師討論，總覺得自己的不足與愚昧，往往卡住在某個細節，卻失去了整個研究的宏觀的觀點。在這兩年多的訓練裡，老師總是不斷的提醒我，身為一個研究生應該有的態度與看法。雖說完成了一本碩士論文，但實在是不覺得自己真的學會了如何做好學術研究，但至少在老師的帶領下，自己或多或少也有了一些長進。真的非常感謝孫啟光老師。

這本論文的完成也要感謝口委老師們的寶貴意見與指正，感謝中研院應科中心的施閔雄教授、凝態中心的張玉民教授、以及應力所的吳政忠教授，讓這本論文能更趨於完整。另外非常感謝施閔雄老師以及施老師實驗室幫忙長樣品的學長姐們，如果不是學長姐的幫忙，這個研究不會有現在的結果。

接著感謝在超快光學實驗室的大家:昱傑學長，是我們奈米組的大學長，當初自己剛進入實驗室時，學長教會了我很多東西，從學長身上，我也學到了做研究的思考邏輯與推敲的一點皮毛。不得不說，學長真的很厲害。感謝建誠學長，第一次在奈米柱實驗上的成功，是跟學長一起的熬夜接力實驗，還有尤其感謝學長在最後的交接以及在文章上的幫忙。感謝阿賓哥，在製程與樣品的資訊上，給了

相當多的寶貴意見，如果不是學長幫忙照關鍵樣品的 SEM，可能現在自己還不知道該怎麼辦，真得非常感謝。感謝後來加入實驗室的 P.A.，如果不是學長的幫忙，自己在 OPO 的實驗不會這麼順利，也感謝 P.A.每次都很有耐心聽我用破英文在討論事情，在奈米柱的討論上，P.A.給了相當多的意見，這點讓我非常感謝。阿胖學長，還好每次熬夜做實驗時，你都還在，還可以一起找喝咖啡吃消夜，讓每次熬夜孤單做實驗的我還感覺有一個伴。還有思齊，昭勳，任棠，子芳，在同屆裡，我真的覺得自己是最弱的一個，大家真的都很厲害，也祝福思齊和子芳的博士班能夠順利，昭勳畢業後可以做自己想做的事，任棠能夠順利出國。孝倫，真是不好意思，自己身為學長卻沒有好好帶你，反倒是你在研究上一直幫助我，真的非常感謝。也非常感謝怡如在課業上還是實驗時間上的大方幫助。還有 Rebecca，感謝妳總是跟我們站在一起在面對教授，蕾姐的關心與打氣，在最後的低潮時期，給了我相當大的鼓勵，最後還有實驗室的其他大家，真的非常感謝，在研究所的兩年多，其實自己真的很少參與大家的活動，感謝大家還這麼的包容我，還願意給我這麼多的幫助。能夠認識各位，實在是自己的福氣。

另外還有感謝俊儒，熊，郭老大，雖然不是同實驗室的，但卻也給了我很多的關懷與幫助。紫微姐，是個好相處的人，總是願意拿出甜心卡讓大家分享，祝福妳在未來的工作能有好的發展。幾米，雖然覺得你很兇，但是其實內心是個好人。湯湯，在後來雖然很少聯絡，但至少很高興曾經有你相伴的日子。翁左庭和柳中原，非常感謝你們一直對我的包容，在你們面前，我總是厚著臉皮的尋求你們的幫助，你們也總是不厭其煩的伸出援手，在這兩年的有很多的難過與開心，身為最好的朋友，你們給了我很大的力量。老呂，感謝你的 Ansys 教學，腦包民，和老褚，感謝你們帶給我的搞笑和樂觀，最後還有施哥，讓台南也能成為我心情

難過時的避風港之一。

佩吟，感謝在這兩年來一直的幫我加油與打氣，妳教會我很多事情，妳的樂觀，總是能讓沮喪的我很快恢復，有妳的陪伴，應該是我多輩子修來的福氣。還有特別感謝高中的班導鄧金城老師，雖然畢業了六年多，但老師還是很關心我們這群已畢業的小毛頭們，老師一直是我心靈上的支柱之一。最後要感謝的是我的家人，我的爸爸，奶奶，你們無怨無悔的付出，並且總是支持我的決定。在我最低潮的時候，才真的發現，家人是我真正的依靠，是支持我的最大力量。念完這兩年多，才發現要感謝的人著實太多，這本論文，雖然自己仍覺得不夠完美，但至少自己盡力，這本論文謹獻於所有關心我和幫助過我的人們，還有我最摯愛的家人們。

中文摘要

利用超快光學方式來產生並偵測具奈米尺度波長與次兆赫(sub-terahertz)頻率音波的技術(picosecond ultrasonics) 已廣泛地被用來評估與研究奈米尺度下的物理現象。先前研究中，因忽略邊界效應，激發之音波主要被視為於晶體塊材內傳播的縱波與橫波模態。而另一方面，奈米結構之共振特性(confined acoustic modes)雖亦被大量地探討與研究，然而音波因受奈米結構邊界之侷限而產生離散波導模態(guided modes)與特定色散關係的傳播特性卻鮮少被討論。故在此研究內，我們欲利用激發探測法(pump-probe technique)，以具奈米厚度之金膜吸收激發光(pump beam)而熱膨脹，進而產生奈米等級波長之音波在砷化鎵奈米柱內以波導模態傳播，再以探測光(probe beam)偵測其反應。在理論計算上，我們用發展於共振超音波頻譜分析(resonant ultrasound spectroscopy)之計算方法處理砷化鎵奈米柱的非等向性，在假設柱體為無限長，邊界沒有受應力的條件下，可得被侷限在奈米柱內傳播之波導模態的色散關係與特徵場型。而在實驗上，我們對一系列不同尺寸的奈米柱分別在不同的探測光(probe beam)波長下做量測，由實驗結果我們歸納：(1)在探測光波長為 880 奈米，所觀測到的震盪訊號主要來自於柱體的徑向呼吸震動模態 (radial breathing mode)，然而(2)在波長為 1120 奈米的探測光的條件下，柱體直徑小於 300 奈米以下的樣品，所觀測到的震盪訊號主要來自於表面奈米金盤的振動。在此情況下，此訊號同時伴隨著回音的產生。我們推測此震盪訊號的轉變和奈米金盤的侷域表面電漿子共振(localized surface plasmon resonance)有關。藉由其效應，奈米金盤可視為一感測器去偵測由底部反射回來的回音。此回音代表由金盤振動所耦合的波導模態在柱體內的傳播以及在柱底不連續介面的反射行為。

由實驗結果分析，音波在奈米柱內的確呈現出不同於塊材內的傳播行為。且其回音時間符合波導理論預期。同時實驗中也顯示，不同模態因介面不連續所造成的反射率不同，其中我們推估主要激發之低頻模態其反射率為 0.5±0.2。

關鍵字：奈米超音波、超快光學、奈米柱、音波波導模態、共振超音波頻譜分析、色散關係、徑向呼吸模態，侷域表面電漿子共振。

ABSTRACT

Picosecond ultrasonics for its mechanisms of generation, detection and applications has been widely studied. Most of previous studies treated the excited acoustic waves as longitudinal and transverse modes due to the neglect of boundary confinement. On the other hand, using femtosecond lasers to excite the confined acoustic modes of nanostructures were also been discussed greatly, but the acoustic guided modes confined to the nanostructures were rarely discussed. In this thesis, we used ultrafast optical pump-probe technique to generate and detect nano-acoustic waves (NAWs) confined to a GaAs nanorod. In our designed structure, a gold nanodisk that deposited on the top of the nanorod was designed to acts as an opto-acoustic transducer. NAWs are launched for the thermal-induced vibration of the disk, and then the waves evolve to guided modes that propagate inside the nanorod. In theory, continuum linear elastic model – resonant ultrasound spectroscopy (RUS) is adopted for the anisotropic elastic properties of GaAs. Under the assumptions of infinite rod length and stress free boundary conditions, the dispersion relation of guided modes is obtained. From experiment, we concluded the detection sensitivity of acoustic responses of the designed samples depend on the probe wavelength: (1) for near-infrared probe (880nm), the dominating oscillatory signal observed is induced from the radial breathing mode of GaAs nanorods. However, (2) for infrared probe (1120nm) condition, the dominant signal converts into the vibration of nanodisk. Under this scheme, echoes with relatively slow velocity are observed as well. We suggested the intervention of localized surface plasmon resonance (LSPR) should be the key to the change of the signal. With the aid of LSPR, the Au nanodisk is not only a transducer but also a highly sensitive acoustic

detector to detect the returning echo. The roundtrip time of observed echo shows a good agreement with the simulation of the anisotropic waveguide theory. The results reflect the fact that propagation of NAWs confined to nanostructures are different to that in bulk crystal. Additionally, in this thesis we further demonstrated the reflection coefficient of the fundamental mode at the rod-substrate interface is roughly 0.5 ± 0.2, while the other modes of higher frequency suffer lower reflection for the issue of mode matching between the nanorod and the substrate.

Key Words: Nano-acoustic waves (NAWs), ultrafast optic technique, nanorod, guided modes, radial breathing mode, resonant ultrasound spectroscopy (RUS), dispersion relation, localized surface plasmon resonance (LSPR).

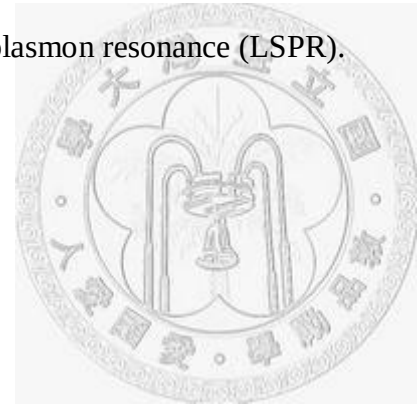

CONTENTS

口試委員會審定書 ..... #

誌謝 i

中文摘要 iv

ABSTRACT vi

CONTENTS viii

LIST OF FIGUREs xi

LIST OF TABLEs xvi

Chapter 1 Introduction 1

1.1 Picosecond Ultrasonic (Nano-Acoustic Waves) 1

1.2 Femtosecond Pump-Probe Technique 2

1.3 Motivation 3

1.4 Thesis Structure 5

Reference 7

Chapter 2 Designed Sample and Experimental Setup 10

2.1 Designed Structure of Samples 10

2.2 Experiment Setup 15

2.2.1 Experiment Setup (probe: 880nm, pump: 440nm) 15

2.2.2 Experiment Setup (probe: 1120nm, pump: 390nm) 17

Reference 19

Chapter 3 Acoustic Dynamics of Laser-Heated Periodic Nanorod Structures .. 20

3.1 Radial Breathing Mode of Nanorods 20

3.2 Surface Acoustic Waves in Surface-Patterned Structures 22

3.3 Backward Brillouin Oscillation 23
3.4 Vibration of Metallic Nano-objects 24
Reference 27
Chapter 4 Nano-Acoustic Guided Waves in Cylindrical Nanorods 29
4.1 Continuum Elastic Theory 29
4.2 Acoustic Waves in Bulk Crystals 31
4.3 Acoustic Waves in Finite Solid – Waveguide Theory 32
4.4 Acoustic Guided Waves in an Isotropic Cylindrical Rod 32
4.5 Acoustic Guided Waves in an Anisotropic Cylinder Waveguide 35
4.5.1 Variation Method 36
4.5.2 Basis Function 37
4.5.3 Classification of Normal Modes 39
4.5.4 Comparison with Pochhammer Chree Theory 40
4.5.5 Dispersion Curve and Mode Distribution of Guided Waves in GaAs NRs 45
Reference 47
Chapter 5 Experimental Results and Discussion 49
5.1 Experiment Results (probe 880nm, pump 440nm) 49
5.2 Experimental Result (probe 1120nm, pump 390nm) 53
5.2.1 Frequency Domain Analysis 56
5.2.2 Detection Mechanism for the Infrared Probe (1120nm) 61
5.2.3 Time Domain Analysis 62
5.2.4 Group Velocity of Acoustic Wave Packet 64
5.2.5 Roundtrip Loss Inside the GaAs Nanorod 69
5.2.6 Backward Brillouin Oscillation 75

Reference 80

Chapter 6 Summary and Future Work 83

LIST OF FIGURES

Fig. 1-1 Schematic diagram of a femtosecond pump-probe experiment 3

Fig. 2-1 Schematic diagram of an Au-attached GaAs nanorod array sample. An Au layer of nano-thickness was deposited onto the top of GaAs nanorod to serve as an opto-elastic transducer. 11

Fig. 2-2 Flow chart of the process for manufacturing Au-attached GaAs nanorods. 13

Fig. 2-3 SEM image of the Au-attached GaAs nanorods array. (a) Side view of the nanorods, the height of the rods is ~720nm from the image, and (b) top view of the nanorods, the diameter is around 340nm from the image. 13

Fig. 2-4 Flow chart of Au-attached GaAs nanorods array. 14

Fig. 2-5 SEM image of the Au-attached GaAs nanorods array. (a) Top view of GaAs nanorod, the diameter is around 256nm, and the period is 355nm from the image. (b) Side view, the height is ~ 720nm. (The sample was made by Hsiang-Yu Chou, and the SEM images were taken by Hung-Ping Chen.).. 14

Fig. 2-6 The schematic diagram of the two color reflection pump-probe system for probe:860~920nm, and pump:430~460nm. 18

Fig. 2-7 The schematic diagram of the two color reflection pump-probe system for probe:1150nm (from OPO), and pump:390nm (from tunable modelock Ti-sapphire laser). 18

Fig. 3-1 Displacement field of radial breathing mode of a nanorod. Pure radial expansion and contraction is observed. (Reprinted with permission from [3.4]. Copyright 2010 American Chemical Society.) 21

Fig. 3-2 Schematic diagram of SAWs in the periodic surface-patterned structure. .. 23

Fig. 3-3 Schematic representation of backward Brillouin oscillation. The incident

probe was drawn in oblique for clear illustration. 24

Fig. 3-4 Schematic diagram of generation of NAWs induced from the thickness vibration of metal thin film. 26

Fig. 3-5 Schematic diagram for radial vibration of Au nanodisk induced by the illumination of pump beam. The disk is attached onto a GaAs nanorod. 26

Fig. 4-1 A 1D model for propagation of disturbance along a chain of atoms. The Springs represent the interactions between atoms. 30

Fig. 4-2 Dispersion relation of LA phonon for the 1D atom chain model, and a is the spacing between each atoms..... 30

Fig. 4-3 GaAs (cubic system) slowness surfaces (unit: m^{-1}) in the (001) surface. In the [100] and [010] direction, the corresponding velocities of quasi-longitudinal and quasi-transverse is 4731m/s and 3347m/s, respectively. 31

Fig. 4-4 (a) Schematic diagram of successive reflections of acoustic waves at the free boundary, in which different wave type are represented by different color. (b) Overall lateral distribution that propagates toward the z direction 32

Fig. 4-5 Schematic diagram of the defined parity in displacement u_x and u_y of dilatational modes.. 39

Fig. 4-6 Dispersion relation of a cylindrical waveguide of radius as 340nm and composed of SiO2. The red lines are from Pochhammer Chree theory, a standard solution for an isotropic waveguide. The blue circles are from RUS method..... 41

Fig. 4-7 Displacement fields of (a) mode 1 and (b) mode 2of Pochhammer Chree theory..... 42

Fig. 4-8 Displacement fields of (a) mode 1 and (b) mode 2 of RUS method 43

Fig. 4-9 Displacement fields of (a) mode 3 and (b) mode 4 of RUS method 44

Fig. 4-10 Calculated dispersion relations of a 340nm-diameter GaAs nanorod. The red dot is calculated from Pochhammer Chree equation, and the solid blue line is calculated from RUS method. 46

Fig. 5-1 Transient change in reflectivity of the sample induced by the pump beam (880nm). A small oscillatory signal that is attributed to coherent phonon generation of the sample is highlighted in the figure. The inset shows the full measured trace. 49

Fig. 5-2 Frequency spectra of 340nm-diameter nanorod samples. 52

Fig. 5-3 Size dependency of the dominating frequency under 880nm probe used ... 52

Fig. 5-4 Transient reflectivity change traces of different sample of different diameter and period under 1120nm probe used 53

Fig. 5-5 Transient reflectivity change of the sample of 239nm-diameter and 355nm-period for (a) infrared (1120nm) probe and (b) near-infrared (880nm) probe. (each trace was normalized by its minimum value) 54

Fig. 5-6 (a) Background-substration oscillatory signal of the sample of 256nm diameter and 355nm period. (b) The signal of the sample of 239nm-diameter and 355nm-period. 55

Fig. 5-7 Frequency spectra of the signal at different timeframe: Black line is full oscillatory signal, red line is that of initial oscillation, and blue line is that of echo signal. (a) The signal of the sample of 255nm-diameter and 355nm-period. (b) The signal of the sample of 239nm-diameter and 355nm-period. Note: Zero padding was used to make the length of each data equal to fairly compare 56

Fig. 5-8 Frequency spectra of the signal of the sample of 180nm diameter for 880nm

probe (black-square line) and 1120nm probe (red-circle line). The dominating peak in red-circle line represents the radial breathing mode of GaAs nanorods. 57

Fig. 5-9 Frequency spectra of the signal of the sample of 250nm diameter for each 880nm probe (black-square line) and 1120nm probe (red-circle line). The dominating peak in red-circle line represents the radial breathing mode of GaAs nanorods. 57

Fig. 5-10 Dominating frequency versus the diameter of the rod under 1120nm probe. 58

Fig. 5-11 The measured trace of transient change in reflectivity of the sample of 256nm diameter and 355nm period.(The frequency of the oscillation highlighted is around 52GHz) 59

Fig. 5-12 (a) SEM image of the Au-attached GaAs nanorods. In this figure the thickness of metal layer can be identified as ~27nm. The graph is taken by Hung-Pin Chen who is a member of our group. (b) Schematic diagram of lateral and thickness vibration of a nanodisk. 60

Fig. 5-13 Dimensionless dispersion relation of an acoustic cylindrical waveguide with infinite length (made of GaAs). The horizontal dashed line represents the dimensionless excitation induced by the lateral vibration of the Au nanodisk. 63

Fig. 5-14 Displacement field distribution of excited guided modes (Mode 1). (The pattern is drawn at the crossing points in the dispersion curve which is shown in Fig. 5-13.)..... 65

Fig. 5-15 Displacement field distribution of excited guided modes (Mode 1). (The pattern is drawn at the crossing points in the dispersion curve which is shown in Fig. 5-13.)..... 66

Fig. 5-16 Simulation of the excited wave packet propagation by considering the dispersive behavior of the fundamental guided mode (mode 1). (The simulation does not consider any loss.) 66
Fig. 5-17 Simulation of the single and the double roundtrip echo. (The simulation does not consider any loss for the echos.)..... 67
Fig. 5-18 Schematic diagram for the echoes observed in experiments..... 68
Fig. 5-19 Fitted result of the data. (Diameter:231nm, period 355nm)..... 70
Fig. 5-20 Fitted result of the data. (Diameter:273nm, period 355nm)..... 70
Fig. 5-21 (a) Background-removed oscillatory signal of 273nm-diameter sample (probe:1120nm). (b) Corresponding frequency spectra of the signal and the noise. 73
Fig. 5-22 Schematic diagram of (a) the mode with major component in axial direction and (b) the mode with major component in radial direction 74
Fig. 5-23 Background-removed oscillatory signal of 440nm-diameter sample (probe:1120nm). (b) Corresponding frequency spectrum..... 75
Fig. 5-24 (a) Background-removed oscillatory signal of 340nm-diameter sample. (b) Corresponding frequency spectrum. (Probe:1120nm) 76
Fig. 5-25 Backward Brillouin oscillation induced by fundamental mode that satisfying the phase matching comditon 77
Fig. 5-26 Schematic diagram of explanation of the strength of the detected backward Brillouin oscillation signal 79

LIST OF TABLES

Table 2-1 Detailed information of samples used in this thesis 11

Table 4-1 Classification of normal modes 39

Chapter 1 Introduction

1.1 Picosecond Ultrasonic (Nano-Acoustic Waves)

Picosecond ultrasonic for its wide applications in physics and engineering has attracted many attentions in recent years. From the first paper reported in 1984, C. Thomsen et al. [1.7] discovered the extremely short time (~ps) oscillation in transient change of transmission and reflection of probe light when the picosecond pump-probe experiment was conducted on thin films of $a-As_2Te_3$ and cis-polyacetylene $(CH)_x$. They attributed the observed oscillations to the generation and the propagation of GHz coherent acoustic phonons which perturb the optical properties of the sample, and they developed a physical model to interpret the mechanisms of generation and detection of coherent acoustic phonon in a later paper [1.6] in 1986.

In a conventional pulsed ultrasonic system, a coherent acoustic pulse is generated by the application of an electric pulse to a suitable transducer, in such an experiment the time resolution is limited by the overall bandwidth of the system. This bandwidth is determined by the mechanical characteristics of the transducer and the electric bandwidths of the generating and the receiving system. The limited time resolution of the system has been proven to be the level of nanosecond (10^{-9} sec), however it is still clearly inadequate to study the character of nanostructures for its limited spatial resolution (several microns). Unlike the conventional ultrasonic system, picosecond ultrasonic technique exhibits the nano-resolution ability in space for the acoustic pulses generated with very short spatial extent around 10nm~100nm (therefore it is also called nano-acoustic waves (NAWs) [1.16]) and for the high resolution in time scale of the femtosecond laser system. This technique was mostly used for nondestructive detection evaluation (NDE) in nanostructures, like thickness estimation of an ultra-thin films by

measuring arrival time of returning echoes [1.4][1.10] and bonding evaluation of interfacial surfaces [1.2] due to a lower transmissivity of acoustic energy for a poor bonding, and so on. In fundamental physics, the generation and the propagation of NAWs are closely related to mechanical and physical properties of nanostructures [1.1] and nanodevices, therefore the studies like sound velocity measurement [1.10], the attenuation measurement of high frequency phonon [1.8][1.9], phonon-carrier interaction, and carrier diffusion [1.11] have been investigated on several semiconductors and metals.

With the increasing investigation and developments of NAWs, it actually provides researchers and scientists a powerful tool on the study of nano-device physic and novel implementation of nano-engineering.

1.2 Femtosecond Pump-Probe Technique

The continuous improvement in ultrafast laser technology have led to many new and fascinating applications in physics, engineering, chemistry, and biology. With these progresses, ultra-short laser pulse width well below 1 picosecond has been achieved. One of these applications is ultrafast pump-probe technique, which is widely used to study the ultrafast phenomenon in semiconductors and metals, such as carrier dynamic [1.18][1.19] and coherent GHz~THz acoustic phonons effect.

Fig. 1-1 shows the schematic diagram of a typical femtosecond pump-probe system. An optical pulse with its width well below 1ps is generated by a femtosecond laser, and then it is divided into two beams for different purposes: the sample is excited by one pulse (pump beam), whereas the transient changes of the sample induced by the pump beam are probed by the other pulse (probe beam). The time delay between pump

and probe is controlled by a delay stage which provides variable optical path difference, thus the transient optical properties change of the sample at different time delays can be recorded with the time scale shorter than 1ps. In the past studies [1.6][1.20][1.21], the ultrafast pump-probe technique has been proven to be a efficient way to generate and detect GHz~THz coherent acoustic phonons in many materials. Therefore, in this thesis, a two-color pump-probe experiment was employed to study ultrafast acoustic responses of the designed samples and to investigate coherent acoustic waves which are generated and guided in GaAs noanrods.

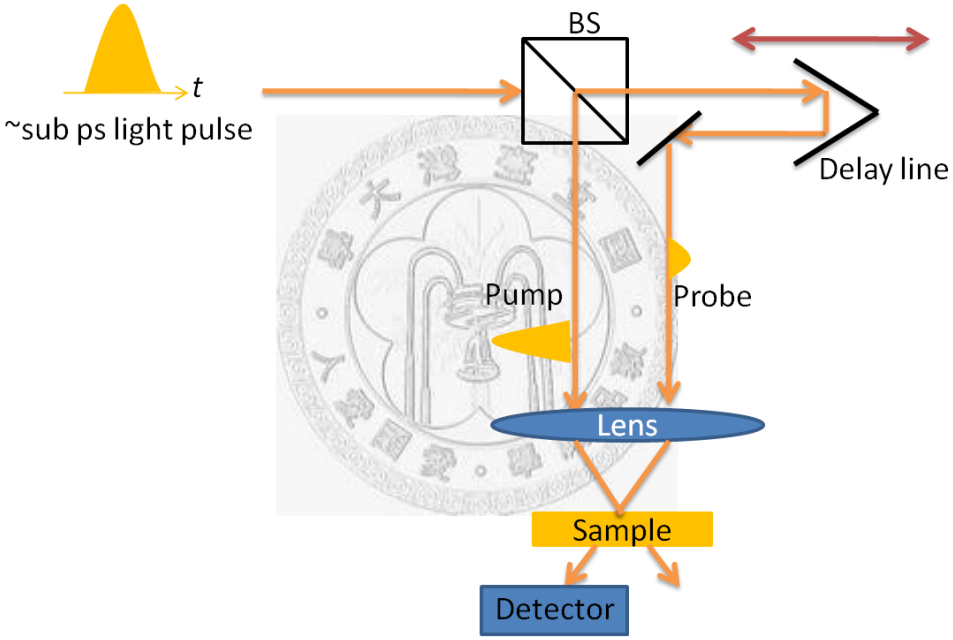

Fig. 1-1 Schematic diagram of a femtosecond pump-probe experiment

1.3 Motivation

In the view of wave propagation, a finite solid structure, like a rod or a plate, can be viewed as a waveguide that directs acoustic waves to propagate toward a specific direction. Dispersive behavior and field distribution of discrete guided modes are quite different as compared to plane waves in a bulk crystal. However, in previous studies, owing to the spot size (~20 μm) of focused optical pulses (pump) is much greater than

the optical absorption depth (~10nm), the excited acoustic waves were treated like that propagate inside a bulk crystal without seeing the boundary (for the lateral size of sample was usually much greater than the spot of NAWs) and diffraction (near field approximation for less than few μm propagation distance), thus the guided effect was neglected and the propagation could be simply modeled as a 1D problem. On the other hand, despite the confined acoustic modes of nanostructures are reported, such as nanodot [1.25], nanorod[1.3][1.22], nanoprism[1.23], nanobshell[1.23] and nanocubes [1.24], how the acoustic waves propagate within the nanostructure has not been revealed.

Recently, one-dimensional materials such as nanowires have attracted considerable attention due to their potential application in energy conversion devices. When crystalline solids are confined to nanometer range, phonon transport within them would be significantly altered due to various effects, namely (1) increased boundary scattering, and (2) modification on phonon dispersion relation. Theoretical studies have suggested that, as the wire diameter is smaller than the phonon mean free path (MFP), the dispersion relation should be modified due to the confinement, for example the phonon group velocity would be significantly less than that in bulk.

Furthermore, when the phonon transport fall into ballistic regime, the thermal conductivity exhibits the quantization. Under this scheme, the wave's properties that are treated as guided waves in these low-dimensional nanostructures are necessary to be taken into consideration. A lot of theoretical studies have calculated the transmission properties of guided modes at the abrupt junction and proposed that thermal conductance could be modified by the shape discontinuity. However, the related experimental work has not been reported as well.

In the low temperature limit, thermal transport are dominated by the lowest

acoustic modes, this frequency range (GHz to sub THz) can be achieved by the usage of picoseconds ultrasonic techniques. Therefore, the study of guided NAWs might provide another viewpoint to investigate the novel thermal properties between low-dimensional structures.

In addition, the dispersive effect resulted from lateral confinement is relatively significant. This makes investigation possible on picosecond nonlinear acoustics, i.e. acoustic soliton, a wave packet propagates with stationary shape in space and a constant velocity for the balance between nonlinearity and dispersive effects [1.12].

Finally, as an analogy to optical systems, the developed bulk NAWs systems so far still lacks an important component: waveguide. Therefore, we proposed the nanorod to serve as a candidate for waveguide utility in nano-ultrasonic imaging, sensing, and other nano-acoustic devices.

Being the first stage of these aims, the investigation of guided NAWs in a nanorod is necessary and impotant. Therefore it is studied and discussed in this thesis.

1.4 Thesis Structure

In this thesis, we studied the guided NAWs confined to a GaAs nanorod by the usage of two-color femtosecond pump probe technique that excites and detects NAWs in our designed samples. Time-resolved oscillations observed in experiments are discussed and compared with an anisotropic waveguide theory of continuum elasticity and other possible acoustic responses of the designed samples. The thesis is organized as follows:

To understand the nature of signal observed, rod size and probe wavelength are controlled as variables in the experiments. Therefore, Chapter 2 gives the information

about designed samples and the detail of two experimental setups used for different probe wavelength with respect to near infrared (880nm) and infrared (1120nm) region. In Chapter 3, the author described some other possible acoustic dynamical responses that has been found to play a role in the nanorod array samples. For quantitative elucidation to guided NAWs, Chapter 4 introduces continuum elastic waveguide theory of infinite isotropic and anisotropic cylindrical rods.

Chapter 5 gives the experimental results and discussion. It was divided into two parts according to the used probe wavelength. For these different cases, different oscillatory signals and the echoes formed by guided modes were observed. Finally, summary and future work of this work are given in the last chapter of this thesis.

Reference

[1.1] B. Bonello, B. Perrin, E. Romatet, J.C. Jeannet, "Application of the picoseconds ultrasonic technique to the study of elastic and time-resolved thermal properties of materials" *Ultrasonic,* **35**, 223 (1997).

[1.2] G. Tas, J.J. Loomis, H.J. Maris, A.A. Balies and L.E. Seiberling. "Picosecond ultrasonics study of the modification of interfacial bonding by ion implantation." *Appl. Phys. Lett.* **72**. 2235 (1998).

[1.3] M. Hu, X. Wang, G. Hartland, P. Mulvaney, J. Juste, and J. Saders, "Vibrational response of nanorods to ultrafast laser induced heating: Theoretical and experimental analysis," *J. Am. Chem. Soc*, **125**, 14925 (2003).

[1.4] H.N. Lin, R.J. Stoner, H.J. Maris, "Nondestructive testing of microstructures by picosecond ultrsonics," *J. Nondestruct. Eval*. **9**, 239 (1990).

[1.5] G.A. Antonelli and H.J. Maris, S.G. Malhotra and James M.E. Harper, "Picosecond ultrasonic study of the vibrational modes of a nanostructure," *J. Appl. Phys.*, **91,** 3261 (2002).

[1.6] C. Thomsen, H. T. Grahn, H.J. Maris and J. Tauc, "Surface generation and detection of photons by picoseconds light pulses," *Phys. Rev. B.*, **34**, 4129 (1986.)

[1.7] C. Thomsen, J. Strait, Z. Vardeny, H.J. Maris and J. Tauc, "Coherent phonon generation and detection by picoseconds light pulses," *Phys. Rev. Lett.*, **53**, 989 (1984).

[1.8] T.C. Zhu, H.J. Maris, and J. Tauc, "Attenuation of longitudinal-acoustic phonons in amorphous SiO2 at frequencies up to 440GHz," *Phys. Rev. B.*, **44**, 4281 (1991).

[1.9] H.N. Lin, R.J. Stoner, H.J. Maris and J. Tauc, "Phonon attenuation and velocity measurements in transparent materials by picoseconds acoustic interferometry," *J. Appl. Phys*, **69**, 3816 (1990).

[1.10] O.B. Wright, "Thickness and sound velocity measurement in thin transparent films with laser picoseconds acoustics," *J. Appl. Phys*, **71**, 1617 (1992).

[1.11] O.B. Wright, "Ultrafast nonequilibrium stress generation in gold and silver," *Phys. Rev. B.*, **49**, 9985 (1994).

[1.12] H.Y. Hao and H.J. Maris, "Experiments with acoustic solitons in crystalline solids," *Phys. Rev. B.*, **64**, 064302 (2001).

[1.13] G. Tas and H.J. Maris, "Picosecond ultrasonic study of phonon reflection from solid-liquid interfaces," *Phys. Rev. B.*, **55** 1852 (1997).

[1.14] X.F. Peng, K.Q. Chen, B.S. Zou and Y. Zhang, "Ballistic thermal conductance in a three dimensional quantum wire modulated with the stub structure." *Appl. Phys. Lett.*, **90**, 193502 (2007).

[1.15] Y.C. Wen, J.H. Sun, C. Dais, D. Grutzmacher, T.T. Wu, J.W. Shi, and C.K. Sun, "Three-dimesional phononic nanocrystal composed of ordered quantum dots." *Appl. Phys. Lett.*, **96**, 123113 (2010).

[1.16] K.H. Lin, C.M. Lai, C.C Pai, J.I. Chyi, J.W. Shi, S.Z. Sun, C.F. Chang and C.K. Sun, "Spatial manipulation of nanoacoustic waves with nanoscale spot sizes," *Nature Nanotech.*, **2**, 704 (2007).

[1.17] Y.H. Chen. "Coherent Opto-Acoustic Behaviors of GaAs Nanorods" Master Thesis, (2009).

[1.18] C. Shank, R. Fork, R. Leheny, and J. Shah, "Dynamics of photoexcited GaAs band-edge absorption with subpicosecond resolution," *Phys. Rev. Lett.*, **42**, 112 (1979).

[1.19] D. Kim and P. Yu, "Hot-electron relaxations and hot phonons in GaAs studied by subpicosecond raman scattering," *Phys. Rev. B*, **43**, 4158 (1991).

[1.20] S. Wu, P. Geiser, J. Jun, J. Karpinski, and R. Sobolewski, "Femtosecond optical generation and detection of coherent acoustic phonons in GaN single crystals," *Phys. Rev. B*, **76**, 85210 (2007).

[1.21] C.K. Sun, J.C. Liang, and X.Y. Yu, "Coherent acoustic phonon oscillations in semiconductor multiple quantum wells with piezoelectric fields," *Phys. Rev. Lett.*, **84**, 179 (2000).

[1.22] S.O. Mariager, D.K. Khakhulin, H. T. Lemke, K.S. Kjar, L. Guerin, L. Nuccio, C.B. Sorensen and M.M. Nielsen and R. Feidenhans'l, "Direct observation of acoustic oscillations in InAs Nanowires," *Nano. Lett.*, **10**, 2461-2465 (2010).

[1.23] P. Yu, J. Tang, and S. H. Lin, "Photoinduced structural dynamics in laser-heated nanomaterials of various shapes and sizes," *The Journal of Physical Chemistry C*, 113, 7480 (2009).

[1.24] H. Petrova, C.H. Lin, S. de Liejer, M. Hu, J.M. Mclellan, A.R. Siekkinen, B.J. Wiley. M. Marquez, Y. Xia, J.E. Sader, G.V. Hartland, "Time-resolved spectroscopy of silver nanocubes: observation and assignment of coherently excited vibrational modes," *J. Am. Chem. Soc.*, **126**, 094709 (2007).

[1.25] T.D. Kruss and F.W. Wise. "Coherent acoustic phonon in a semiconductor quantum dot." *Phys. Rev. Lett.*, **79**, 5102-5105 (1997).

Chapter 2 Designed Sample and Experimental Setup

2.1 Designed Structure of Samples

To study guided NAWs in the nanorod, the source of generation of NAWs is needed. Therefore, we would like to briefly introduce the generation mechanisms here and then give the reason why the structure of sample was designed.

From the past abundant researches and studies, the ways to generate NAWs in metals and semiconductors by optical excitation can be roughly classified as below:

(1) Thermal stress [2.1]: the optical-absorbing region suffers instant thermal expansion due to rapid temperature rise resulted from strong absorption of femtosecond light pulses, and thus launch acoustic waves outward.

(2) Deformation potential [2.1][2.2]: it is one of dominating mechanisms for phonon generation in semiconductors. Since the generation of electron-hole pairs excited by optical pulses would introduce an electronic stress to perturb equilibrium status of the lattice. (Valance band electrons in general help to bind the lattice more effectively than the conduction electrons)

(3) Piezoelectric effect: it has been reported to be an efficient way to generate high-amplitude coherent sub-THz phonon compared to the other mechanisms [2.4]. By using highly strained quantum well structures, NAWs are generated via piezoelectricity for excited electrons and holes are separated by original built-in electric field, and then introduce an additional field that perturbs the equilibrium status of lattices. This technique has been used for manipulation of NAWs pulse shape and frequency spectrum [2.4], etc.

For these mechanisms discussed above, the simplest way to generate NAWs in the nanorod is thermal stress. A metallic film of nano-thickness was proposed to be used as

a better transducer for its high optical absorption that can increase temperature rise [2.5]. Therefore, for our samples, an Au layer of nano-thickness was designed to deposit onto the top of the GaAs nanorod to serve as an opto-elastic transducer.

The schematic diagram is given in Fig. 2-1. Detailed information of designed samples used in this thesis is arranged as the following:

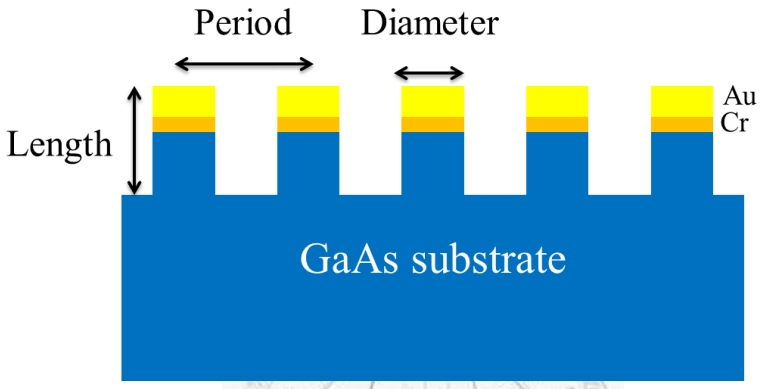

Fig. 2-1 Schematic diagram of an Au-attached GaAs nanorod array sample. An Au layer of nano-thickness was deposited onto the top of GaAs nanorod to serve as an opto-elastic transducer.

Table 2-1 Detailed information of samples used in this thesis

Rod Diameter	340nm	130~200nm	220~270nm	440nm
Rod Length	720nm	720nm	720nm	920nm
Period	500nm	300nm	355nm	620nm
Thickness of Au disk	15~20nm	20~30nm	20~30nm	20~30nm

The samples were provided by Prof. Min-Hsiung Shih (Research Center for Applied Sciences, Academia Sinica). Among these samples, the one of 340nm diameter was grown by Cheng-Wen Cheng, and the other samples were grown by Hsiang-Yu Chou, both are members in Prof. Shih's group. The growing process of these two sets of sample are slightly different while the latter modified the process to better control the

thickness of Au layer and to reduce the over-deposited Au that attaches on the side wall and the bottom of nanorods.

Fig. 2-2 shows the flow chart of sample processing for the 340nm-diameter sample. First, a SiN_X film was deposited on a [100] GaAs wafer by MOCVD (Metal-Organic Chemical Vapor Deposition) and spin coated PMMA (Poly(methyl methacrylate)) on the SiN_X film. Second, use EBL (E-Beam Lithography) to write the patterns of nanorods. After the development, the patterned PMMA film acted as a mask for the SiN_X film. Third, etch the SiN_X film by ICP (Inductively Coupled Plasma). Fourth, lift off the PMMA film and now the patterned SiN_X film acted as a mask for the GaAs wafer, and then etched the GaAs wafer by ICP again. Finally, remove the SiN_X by the B.O.E solution and deposited chromium and gold onto the sample.

For the other samples (samples of diameter that are below 300nm and the one of 440nm diameter), the processing is briefly described in Fig. 2-3. The main differences from the former are the pre-deposited Cr (~5nm) and Au layer on the GaAs wafer. Then, the PECVD (Plasma-enhanced Chemical Vapor Deposition) was used to deposit the SiNx onto it, and followed by PMMA layer by spin coating. The remaining processes are the same as the former except an additional step to etch the Cr and the Au by Ar ion milling. Since the Au layer was deposited at first on the GaAs wafer, the homogeneity of deposited Au layer could control better and the over-deposition could be avoided as well.

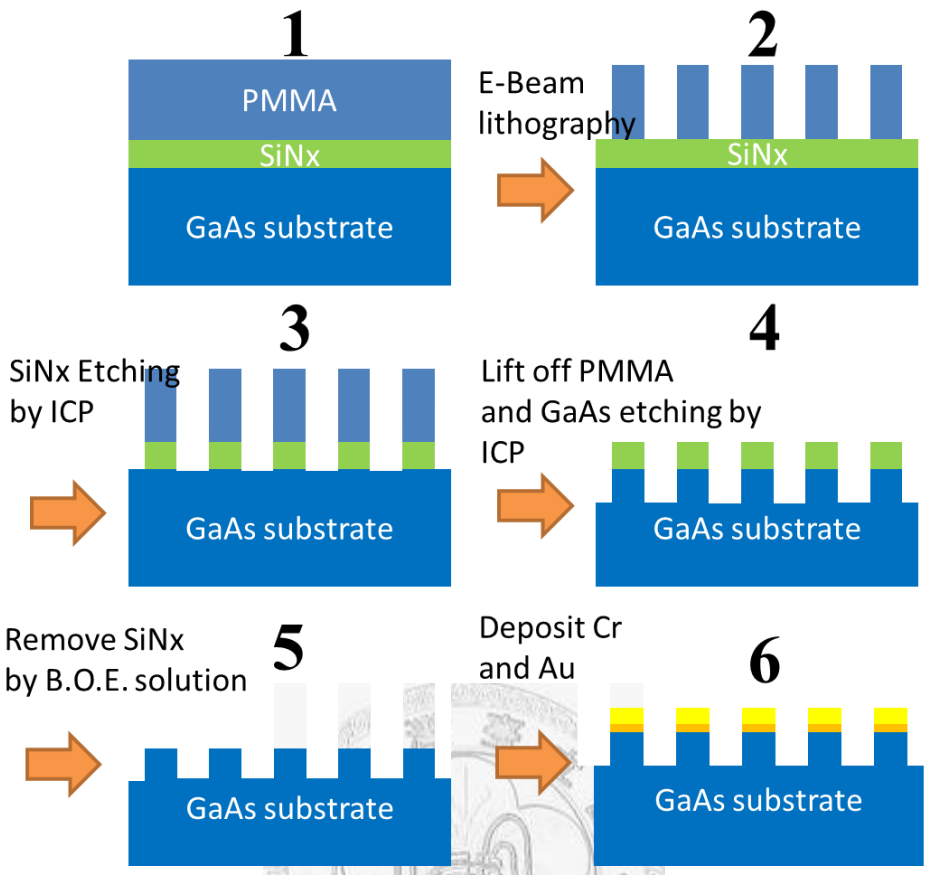

Fig. 2-2 Flow chart of the process for manufacturing Au-attached GaAs nanorods. (the sample was prepared by Cheng-Wen Cheng).

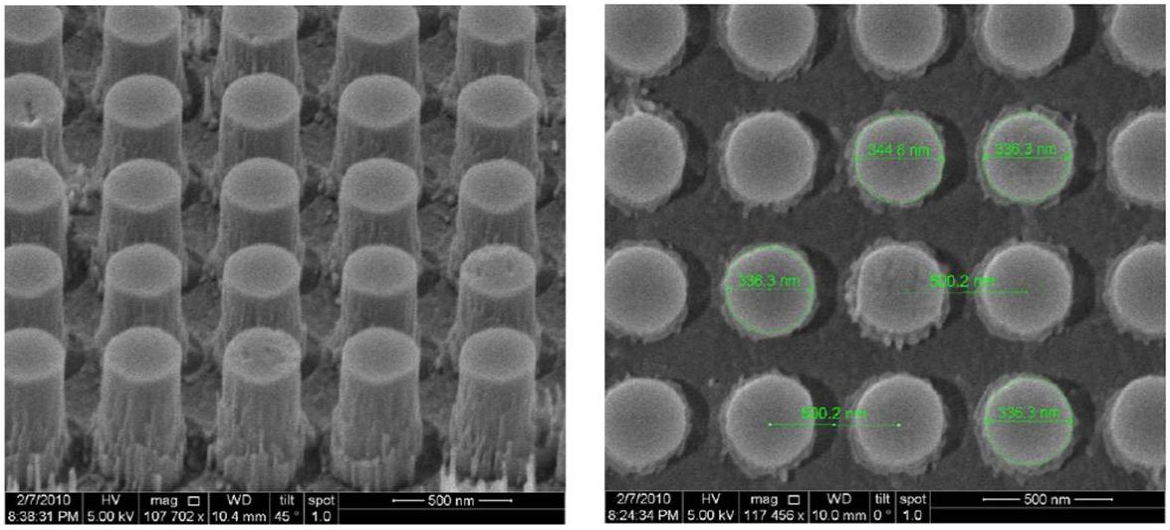

Fig. 2-3 SEM image of the Au-attached GaAs nanorods array. (a) Side view of the nanorods, the height of the rods is ~720nm from the image, and (b) top view of the nanorods, the diameter is around 340nm from the image.

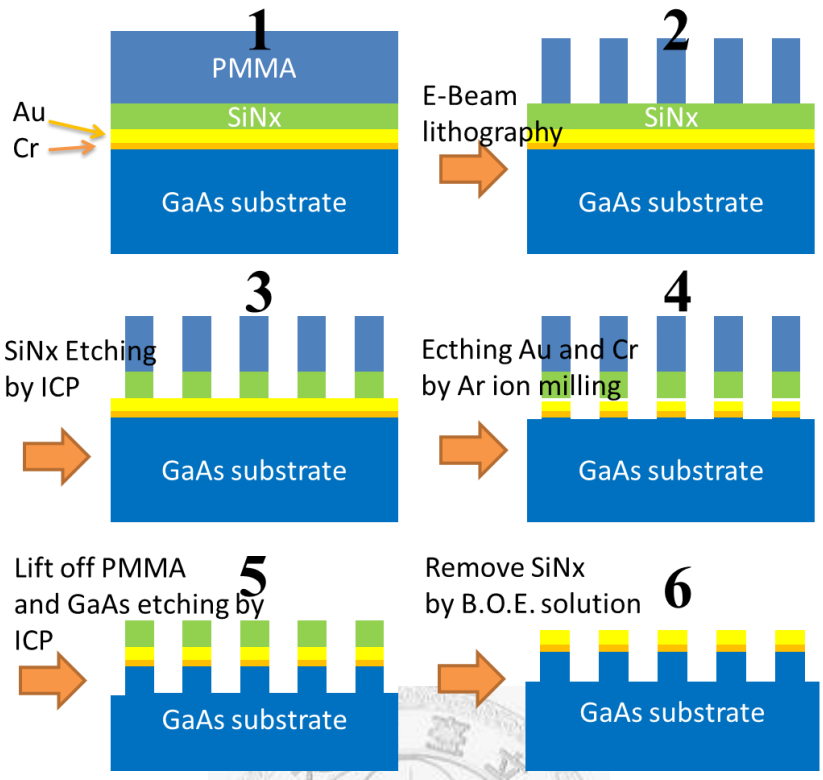

Fig. 2-4 Flow chart of Au-attached GaAs nanorods array. (The samples was prepared by Hsiang-Yu Chou)

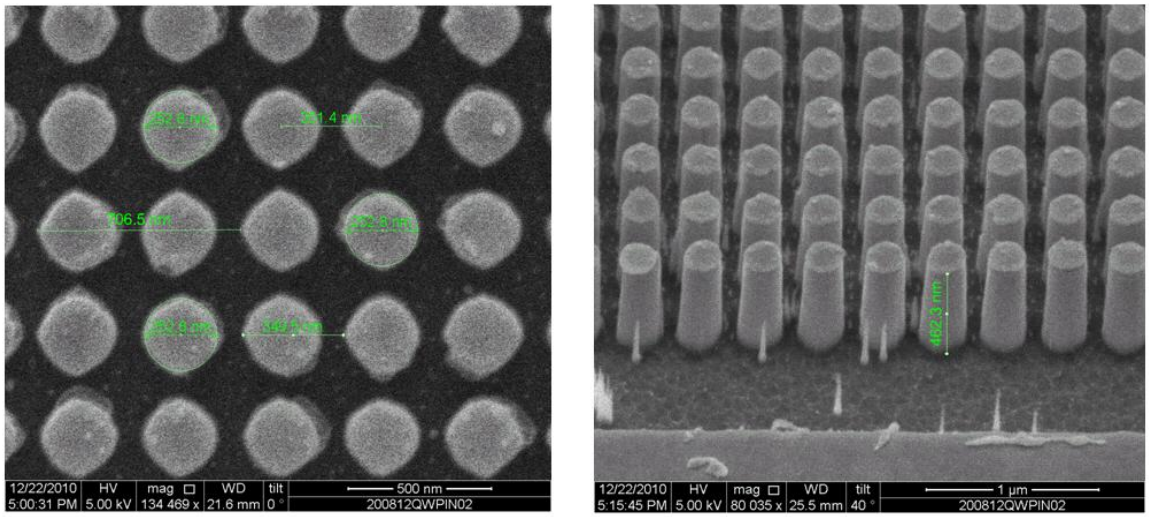

Fig. 2-5 SEM image of the Au-attached GaAs nanorods array. (a) Top view of GaAs nanorod, the diameter is around 256nm, and the period is 355nm from the image. (b) Side view, the height is ~ 720nm. (The sample was made by Hsiang-Yu Chou, and the SEM images were taken by Hung-Ping Chen.)

2.2 Experiment Setup

A two-color reflection pump-probe system was used to study the acoustic dynamic response of Au-attached GaAs nanorods array. Transient change of reflectivity induced by the pump is recorded by the following probe. A wavelength-tunable femtosecond mode-locked Ti:Sapphire laser (Coherent Mira 900) was used to generate laser pulses with its pulse width ~200 femtosecond (10^{-15} sec) and a repetition rate of 76MHz. Due to the demand for different probe wavelengths, two experimental setups were employed with respect to the near infrared (880nm) and infrared region (1120nm). The author would give the details about these two experimental setups in the sections 2.2.1 and 2.2.2.

2.2.1 Experiment Setup (probe: 880nm, pump: 440nm)

In the wavelength range between 700nm to 1 μm, the femtosecond laser (Coherent Mira 900) was used to generated light pulses. The generated beam (880nm) was first separated into two beams by non-polarized power beam splitter, and one with higher power acts as the pump beam, and the other attenuated by a neutral density filter as the probe beam. For the two-color pump-probe system, the pump beam was first focused on a BBO crystal for the second harmonic generation (880nm→440nm), and then it was directed to pass through a color filter to remove the component of fundamental frequency. The pump beam was then collimated and guided into a retro-reflector on a translation stage, which provided controllable optical path difference between the pump and the probe beam. To enhance signal-to-noise ratio (SNR), the pump beam was directed to pass through an acoustic-optic modulator (AOM), which modulate the beam with higher frequency (100 kHz~600 kHz) than the chopper (~1.5 kHz). The modulation frequency of the AOM was chosen for the smallest noise level in electronic

system and always below 500 KHz.

On the other hand, we used a set of telescope to control the divergence of the pump beam so that two beams with different wavelengths can focus on the same focal plane. A lens was used to focus both beams to achieve small spot-size that can be fully located within the nanorod pattern. Moreover, before both beam were focused, they were overlapped collinearly by using a dichroic mirror. In addition, the input power of the pump beam was set to prevent the sample from damage.

The reflection of probe beam was then collected and focused onto the photo-detector through a color filter which effectively removed the scattered pump. Finally, the output signal of the photo-detector was connected to a RF lock-in amplifier (Stanford Research SR-844) which was locked with the same modulation signal of the AOM. The small pump-induced signal was extracted from noise by the RF lock-in amplifier since the modulated pump resulted in a variation of reflection of the probe at the same modulation frequency. We then recorded and averaged the measured traces in a computer as a function of time delay between the pump and the probe beam. Fig. 2-6 shows the schematic diagram of the pump-probe system set up.

2.2.2 Experiment Setup (probe: 1120nm, pump: 390nm)

The wavelength of probe was chosen to be longer to study wavelength dependency of acoustic responses of the samples. Due to the limited wavelength output from the femtosecond Ti-Sapphire laser (700-1000nm), the optical parametric oscillator (OPO) was employed to generate the probe of wavelength above $1\,\mu m$. Femtosecond light pulses with central wavelength of 780nm from the Ti-Sapphire laser were used to pump the OPO, and then the optical parametric down conversion process converted the input beam into two outputs: the "signal" and the "idler". Signal beam is defined by the higher frequency (short wavelength) of the two generated outputs. According to the working principle (nonlinear process) of OPO, signal beam of 1120nm wavelength that was used to probe the samples will be generated. In order to remain the same excitation condition for the sample as possible, the ultraviolet pump is demanded. Therefore the idler beam was filtered and remaining unconverted pumping beam (790nm) was output from OPO cavity and focused onto the BBO crystal to double the frequency (790nm→ 390nm), and then it was used as the pump beam to excite the samples. The different optical path between the pump and the probe beam within the OPO cavity was calculated and compensated in the outside-cavity optical path. Three sets of telescopes were settled in the experiment. Two of them was installed to collimate the two highly-divergent beams when output from the OPO cavity and the other is used to adjust the focal depth of the pump to match the probe beam. The remaining details are the same as previous setup, and the schematic diagram of the system setup is given in Fig. 2-7.

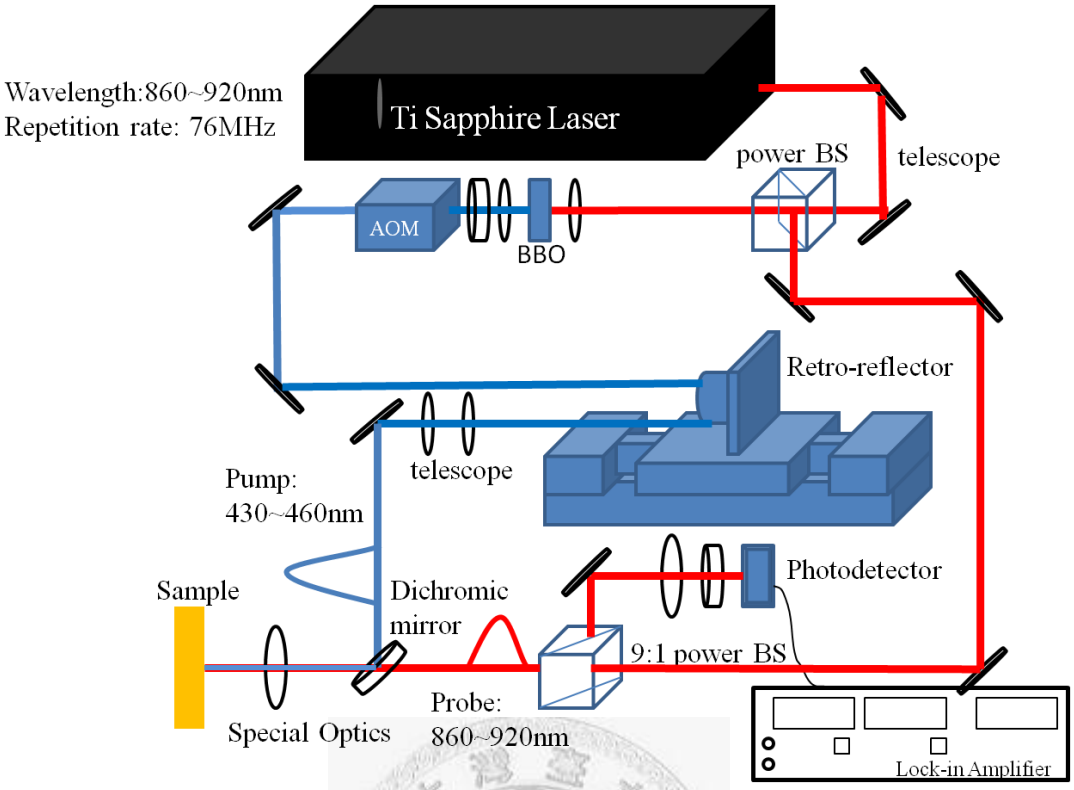

Fig. 2-6 The schematic diagram of the two color reflection pump-probe system for probe:860~920nm, and pump:430~460nm.

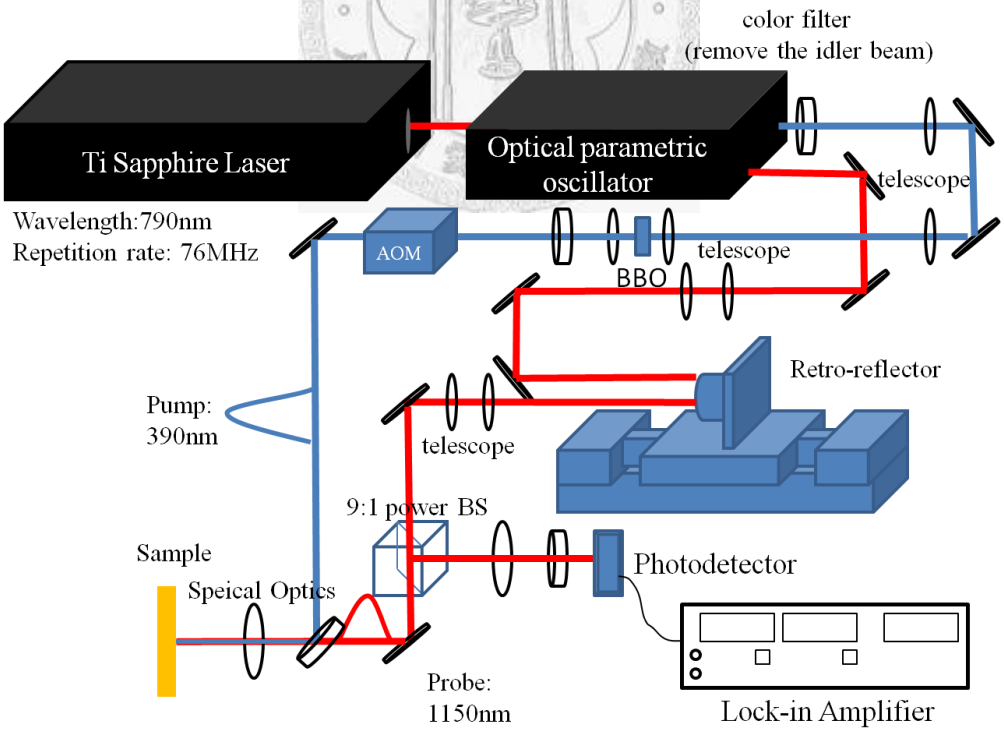

Fig. 2-7 The schematic diagram of the two color reflection pump-probe system for probe:1150nm (from OPO), and pump:390nm (from tunable modelock Ti-sapphire laser).

Reference

[2.1] C. Thomsen, H. T. Grahn, H.J. Maris and J. Tauc, “Surface generation and detection of photons by picoseconds light pulses,” *Phys. Rev. B.*, **34**, 4129 (1986.)

[2.2] O. Matsuda, T. Tachizaki, T. Fukui, J.J. Bauberg and O.B. Wright, “ Acoustic phonon generation and detecton in $GaAs$ / $Al_{0.3}Ga_{0.7}As$ quantum wells with picoseconds laser pulse.” *Phys. Rev. B.*, **71**, 115330 (2005)

[2.3] P. Babilotte, P. Ruello, T. Pezeril, G. Vaudel, D. Mounier, J.-M. Breteau and V. Gusev. “ Transition from piezoelectric to deformation potential mechanism of hypersound phtogeneration in n-doped GaAs semiconductors.” *J. Appl. Phys*, **109**, 064909 (2011).

[2.4] C.K. Sun, J.C. Liang, X.Y. Yu. "Coherent Acoustic Phonon Oscillations in Semiconductor Multiple Quantum Wells with Piezoelectric Fields." *Physical Review Letters* **84**(1): 179. (2000)

[2.5] H.N. Lin, R.J. Stoner, H.J. Maris, “Nondestructive testing of microstructures by picosecond ultrsonics,” *J. Nondestruct. Eval*. **9**, 239 (1990).

[2.6] C. T. Yu, K.H. Lin, C.H. Hsieh, C.C. Pan, J.I. Chyi and C.K. Sun. “Generation of frequency-tunable nanoacoustic waves by optical coherent control.” *Appl. Phys. Lett.*, **87**, 093114 (2005)

Chapter 3 Acoustic Dynamics of Laser-Heated Periodic Nanorod Structures

Despite our samples were designed to study the guided NAWs in the GaAs nanorod, however, from the abundant pump-probe studies about picosecond ultrasonics of periodical nanostructures, we were well aware that there are many mechanisms which would play a role in the present experimental scheme. Therefore this chapter would like to introduce possible acoustic dynamic responses of the periodic Au-attached GaAs nanorod array samples. These mechanisms have been well studied on individual or periodical nanostructures which are similar to our scheme. In the following, mechanisms about breathing mode vibration of a nanorod, surface acoustic waves (SAWs) in surface-patterned structures, backward Brillouin oscillation (interferences between the original reflected probe and an additional one induced by the propagating strain), and acoustic modes of metallic nano-objects would be introduced in detailed.

3.1 Radial Breathing Mode of Nanorods

A number of groups have shown that ultrafast laser excitation of nanoparticles can coherently excite low frequency vibration modes [3.1]. For semiconductors, the above-bandgap excitation changes the dimensions of the unit cell, which can impulsively excite totally symmetric phonon modes (vibrational modes). Symmetric breathing modes possess the nature of being most possibly excited for homogenous optical illumination excitation scheme. Observations of radial breathing modes of slender nanorods ($l/a >> 1$) of metals and semiconductors have been reported in some literatures [3.4][3.5]. Fig. 3-1 shows the displacement pattern of the radial breathing

mode of a rod, a pure expansion and contraction in radial is observed. The detailed mathematical derivation can be found elsewhere [3.4], thus here we only emphasize the assumptions of the model and its analytical result. The natural resonant frequency of the fundamental radial breathing mode of a rod is given by the following formula [3.4]:

$$f_{br} = \frac{\tau}{2\pi a}\sqrt{\frac{E(1-\nu)}{\rho(1+\nu)(1-2\nu)}} = \frac{\tau V_L}{2\pi a}, \tag{3.1}$$

where a is the radius of the rod, E is Young modulus, ν is Poisson ratio, ρ is the mass density, V_L is the longitudinal velocity, and the parameter τ is the fundamental solution of the eigenvalue equation: $\tau J_0(\tau) = \frac{1-2\nu}{1-\nu} J_1(\tau)$ [3.4] (J_0 and J_1 are the zero and the first order Bessel function of first kind, respectively.)

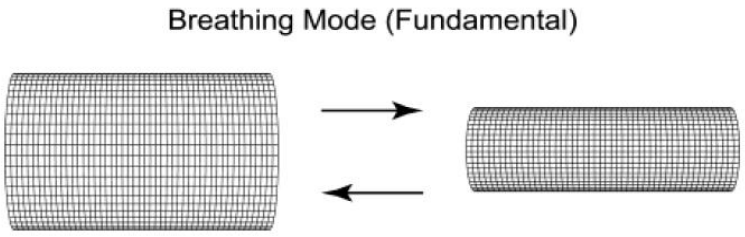

Fig. 3-1 Displacement field of radial breathing mode of a nanorod. Pure radial expansion and contraction is observed. (Reprinted with permission from [3.4]. Copyright 2010 American Chemical Society.)

The model is based on the assumptions of isotropic material and a free cylinder with a high aspect ratio (thus the boundary conditions at the end surfaces can be reasonably ignored). In the present case, although nanorods do stand upon the substrate, which should modify the boundary conditions of the surface, in reference [3.5], Simon O. Mariager et al. has showed the detection of radial breathing mode of InAs nanowires under the pump-probe experimental scheme.

3.2 Surface Acoustic Waves in Surface-Patterned Structures

In a semi-infinite solid, surface acoustic waves (SAWs) is a type of acoustic waves propagating along the surface of an elastic medium. The waves have its amplitude that typically exponentially decays with depth into the substrate and the slower velocity than the body waves. Since a periodic structure provides spatial modulation in surface, SAWs can be excited in a sample with grating or periodic patterns which are fabricated on the surface. D. H. Hurley et al. [3.6] showed the excitation and detection of SAWs of nano-wavelength in a 1D sub-optical wavelength grating structure under the pump-probe experimental scheme. Furthermore, J. F. Robillard et al. [3.7] revealed that there are two kinds of vibration modes in 2D periodic nanocubes: (1) individual resonance modes of a nanocube, and (2) collective modes which represent the coupling between the cubes of the artificial 2D lattice (phononic crystal). The collective modes exhibit strong dependency on the spacing period and possess the dispersive nature of SAWs as the periodic spacing becomes infinite. The frequencies of these surface acoustic modes can be formulated with the Rayleigh wave velocity V_R [3.8] as:

$$f = \frac{V_R}{2\pi} k_{i,j} = \frac{V_R}{a} \sqrt{i^2 + j^2} \,, \tag{3.2}$$

where a is the spacing (periodicity), and (i, j) are integers which represent the wave vectors in a reciprocal lattice. In addition, the paper also reported a phenomenological condition for being able to detect these modes: the probe wavelength is close to or smaller than the periodic spacing of the nanostructure, i.e. $\frac{\lambda}{a} \leq 1$ should be satisfied.

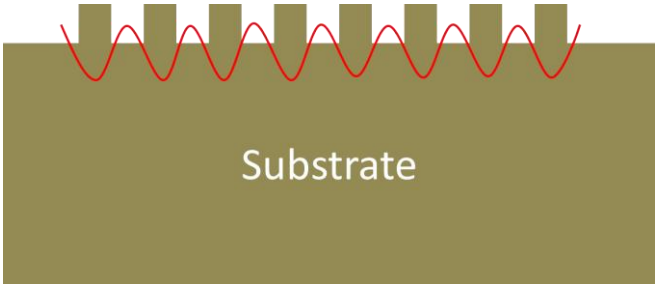

Fig. 3-2 Schematic diagram of SAWs in the periodic surface-patterned structure.

3.3 Backward Brillouin Oscillations

Acoustic disturbance can modulate optical properties of material via the photoelastic effect, which is a phenomenological description of the change of permittivity with a relation of $\Delta\varepsilon = p\eta$, where $\varepsilon = (n + i\kappa)^2$, p is the photoelastic tensor and η is the strain field. Backward Brillouin oscillation is one of optical detection methods for propagating strain field. This mechanism can be understood by considering an acoustic wave as a moving mirror to induce an additional reflected probe [3.9][3.10]. As the acoustic wave propagates, constructive or destructive interference between the original reflected probe and the strain-induced reflected one would alternatively occur, depending on the distance that acoustic wave travels. Thus it makes the transient oscillation in reflectivity of probe with respect to the delayed time.

However, an acoustic pulse is a combination of broad band frequency components, not all the acoustic component can be detected via this mechanism. According to the developed theoretical model [3.9][3.10], only the component which satisfies the "phase matching" can contribute the signal. The condition is given as follows:

$$q = 2nk_0 = 2k = \frac{4\pi n}{\lambda_{pr}}, \tag{3.3}$$

where q, k_0, and k are the wave vectors of the acoustic component, the probe light

in vacuum, and the probe light in the sample, respectively. n is the refractive index, and λ_{pr} is the optical wavelength of the probe in vacuum. The frequency of backward Brillouin oscillation in transient reflectivity contributed by the acoustic component is [3.9]

$$f = \frac{\omega_a\big|_{q=2nk_0}}{2\pi} = \frac{2nV_{ph}}{\lambda_0}, \tag{3.4}$$

where V_{ph} is the phase velocity of the acoustic component, i.e. $V_{ph} = \frac{\omega_a}{q}$. The schematic diagram is shown in Fig. 3-3.

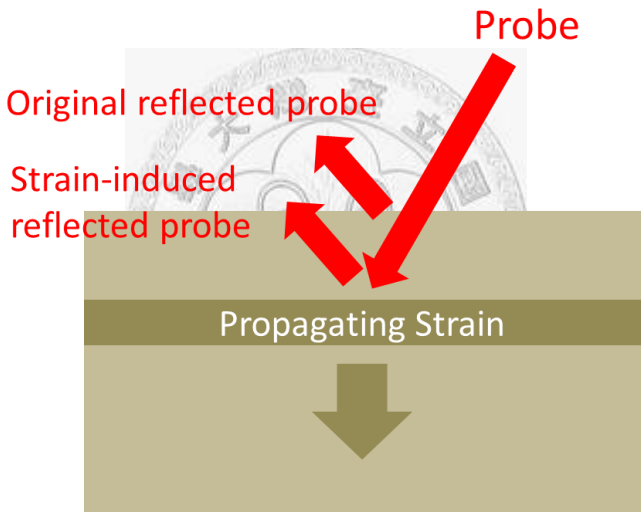

Fig. 3-3 Schematic representation of backward Brillouin oscillation. The incident probe was drawn in oblique for clear illustration.

3.4 Vibration of Metallic Nano-objects

The optical excitation of vibration modes of metallic nano-objects is slightly different to that of semiconductors. In metals, electrons are excited by absorbing optical pulses, and then quickly release their excess energy to the lattice via the electron-phonon coupling in the following picosecond interval. The process thereby

raises the lattice temperature and sets up the thermal stress. In the present sample, the Au nanodisk is expected to be the strongest absorbing part respect to the pump light in the structure, so it could possibly show the response of individual vibration of the nanodisk in the measurement.

Since the shape and the geometry of an object strongly affect its resonant modes, the mode of a thin film and a nanodisk are absolutely different. In the previous studies, typical generation mechanism used a metallic film of nano-thickness as a transducer [3.11][3.12]. Since the film can be viewed as an infinite extent as compared with its thickness, the vibration induced by the thermal expansion of small heated area can be viewed as a 1D problem, as shown in Fig. 3-4. The frequency of thickness vibration can be higher than hundreds of GHz due to successive reflections of acoustic waves at the thickness boundary [3.13]. Therefore the frequency can be simply determined from the formula:

$$f = \frac{V_L}{2d}, \tag{3.5}$$

where d is the thickness of the film, and V_L is the longitudinal velocity in the thickness direction. However, the shape of the transducer used in our case was a disk rather than a film, the characteristic vibration mode is thus different than predicted one of the film. In the previous research, P. Yu et al. [3.14] has investigated the photo-induced structure dynamics of laser-heated metal nanodisks, in which they revealed that under the uniformly heating throughout the disk, the dominant mode that was excited should be the radial mode, and its frequency now depends on its radius rather than thickness. The frequency can be simply determined by:

$$f = \frac{V_L}{2D}, \tag{3.6}$$

where D is the diameter of the disk, and V_L is the longitudinal velocity in the radial direction. The schematic diagram is shown in Fig. 3-5.

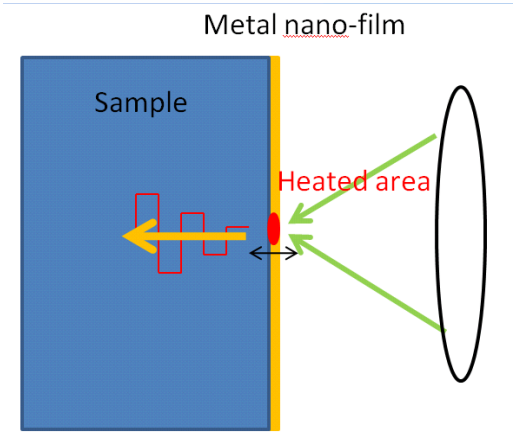

Fig. 3-4 Schematic diagram of generation of NAWs induced from the thickness vibration of metal thin film.

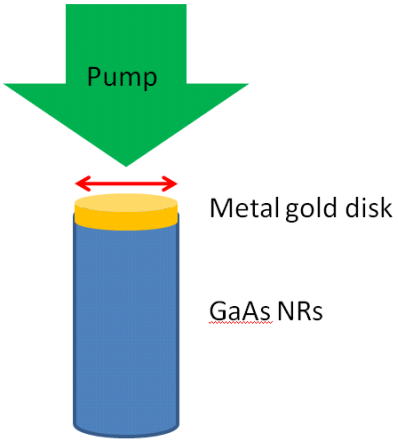

Fig. 3-5 Schematic diagram for radial vibration of Au nanodisk induced by the illumination of pump beam. The disk is attached onto a GaAs nanorod.

Reference

[3.1] G.V. Hartland. "Coherent Excitation of Vibration Modes in Metallic Nanoparticles." *Annu. Rev. Phys. Chem.* **57**, 403 (2006).

[3.2] M. Yamaguchi, J. Liu, D. Ye, and T. M. Lu. "Coherent acoustic vibration in silicon submicron spiral arrays." *J. Appl. Phys* **106**, 033517 (2009).

[3.3] A. Neleta, A. Cruta, A. Arboueta, N. Del. Fattia, F. Valléea, H. Portalèsb, L .Saviotc, E. Duvalb. "Acoustic vibrations of metal nanoparticles: high order radial mode detection." *Appl. Surf. Sci*. **226**, 209 (2004).

[3.4] M. Hu, X. Wang, G. Hartland, P. Mulvaney, J. Juste, and J. Saders, "Vibrational response of nanorods to ultrafast laser induced heating: Theoretical and experimental analysis," *J. Am. Chem. Soc*, **125**, 14925 (2003).

[3.5] S.O. Mariager, D.K. Khakhulin, H. T. Lemke, K.S. Kjar, L. Guerin, L. Nuccio, C.B. Sorensen and M.M. Nielsen and R. Feidenhans'l, "Direct observation of acoustic oscillations in InAs Nanowires," *Nano. Lett.*, **10**, 2461-2465 (2010).

[3.6] D. H. Hurley and K. L. Telschow. "Picosecond surface acoustic waves using a suboptical wavelength absorption grating." *Phys. Rev. B*, **66**, 153301 (2002).

[3.7] J.-F. Robillard, A. Devos, and I. Roch-Jeune. "Time-resolved vibrations of two-dimensional hypersonic phononic crystals." *Phys. Rev. B*, **76**, 092301 (2007)

[3.8] J.-F. Robillard, A. Devos, I. Roch-Jeune, and P. A. Mante. "Collective acoustic modes in various two-dimensional crystals by ultrafast acoustics: Theory and experiment." *Phys. Rev. B*, **78**, 064302 (2008).

[3.9] C. Thomsen, H. T. Grahn, H. J. Maris and J. Tauc. "Picosecond interferometeric technique for study of phonons in the brillouin frequency range." *Opt. Commun.*, **60**, 55 (1986)

[3.10] R. Liu, G.D. Sanders C.J. Stanton, C. S. Kim, J.S. Yahng, Y.D. Jho, K. J. Jho, K. J. Yee, E. Oh, and D. S. Kim. “Femtosecond pump-probe spectroscopy of propagating coherent acoustic phonons in $In_xGa_{1-x}N/GaN$ heterostructures.” *Phys. Rev. B.*, **72**, 195335 (2005)

[3.11] A. Devos and R. Côte. “Strong oscillations detected by picosecond ultrasonics in silicon: Evidence for an electronic-structure effect.” *Phys. Rev. B.*, **70**, 125208 (2004)

[3.12] Y. C. Wen, J. H. Sun, C. Dais, D. Grützmacher, T. T. Wu, J. W. Shi, and C. K. Sun. “Three-dimensional phononic nanocrystal composed of ordered quantum dots.” *Appl. Phys. Lett.* **96**, 123113 (2010).

[3.13] H.N. Lin, R.J. Stoner, H.J. Maris and J. Tauc, “Phonon attenuation and velocity measurements in transparent materials by picoseconds acoustic interferometry,” *J. Appl. Phys*, **69**, 3816 (1990).

[3.14] Yu, P., J. Tang, et al. "Photoinduced Structural Dynamics in Laser-Heated Nanomaterials of Various Shapes and Sizes." *The Journal of Physical Chemistry C* **113**(17): 7480-7480 (2009).

Chapter 4 Nano-Acoustic Guided Waves in Cylindrical Nanorods

4.1 Continuum Elastic Theory

Materials, such as solids, liquids and gases, are composed of atoms separated by empty space. However, macroscopic physical phenomena are usually modeled assuming the materials as a continuous medium, meaning the matter in the body is continuously distributed and fills the entire region of space it occupies. For the study of elastic behavior of solids, stress, expressed as force per unit area, is a measure of internal force of a deformable body. Strain, representing the deformation, is expressed as displacement per unit length. Both strain and stress are second rank tensors σ_{ij}, ε_{ij} in the three-dimensional elasticity theory. Each tensor has 9 components for describing the normal and the shear parts. Constitutive equation, $\sigma_{ij} = C_{ijkl}\varepsilon_{kl}$, known as a generalized form of Hooke's law, describes the relation between stress and strain. The relation is governed by a fourth rank tensor C_{ijkl} (stiffness tensor) which is determined from the crystal properties.

However, when the wavelength of acoustic waves becomes smaller than nano-scale and the frequency becomes higher than THz, the concept of energy quanta of vibration called phonons has to be introduced for quantum effect consideration. According to a simple model which places the equivalent springs between each atoms, as shown in Fig. 4-1, we can simply derive its dispersion relation [4.1] [4.4]. For a 1D diatomic model, phonons are classified into two types according to its different dispersive behaviors: longitudinal acoustic (LA) and longitudinal optical (LO) phonons. For a more general 3D model, transverse phonons i.e. TA and TO, will be included. Dispersion curve of the

1D model is sketched in Fig. 4-2. The interval of $-\frac{\pi}{a} < k < \frac{\pi}{a}$ is called the first Brillouin zone. It is obvious to see the strong dispersive behavior of acoustic phonons near the zone edge since the wavelength is comparable to interatomic distance. In this extreme case, the continuum elasticity is not available anymore, because the definitions of stress $\sigma = \lim_{\Delta A \to \infty} \frac{\Delta F}{\Delta A}$ and strain $\varepsilon = \lim_{\Delta r \to \infty} \left[\frac{u(r+\Delta r) - u(r)}{\Delta r} \right]$ are under the assumption that the solid is continuous in space so the derivative becomes meaningless. Because of the failure to apply continuum elasticity in such a small spatial scale, numerical approaches based on atom or molecular dynamics are usually used for the investigation of the acoustic dynamic behavior of nano-scale structures [4.3].

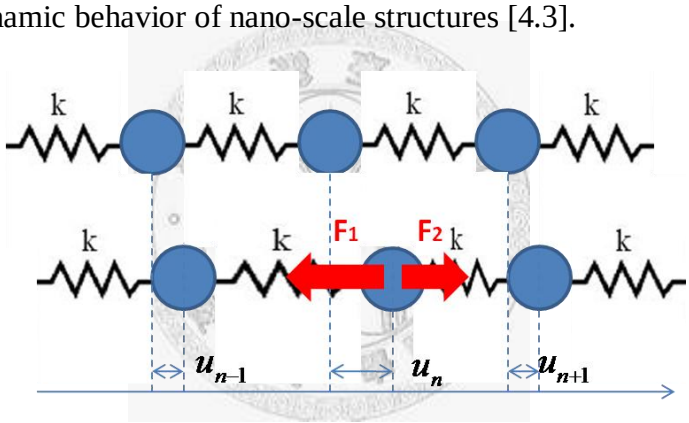

Fig. 4-1 A 1D model for propagation of disturbance along a chain of atoms. The Springs represent the interactions between atoms.

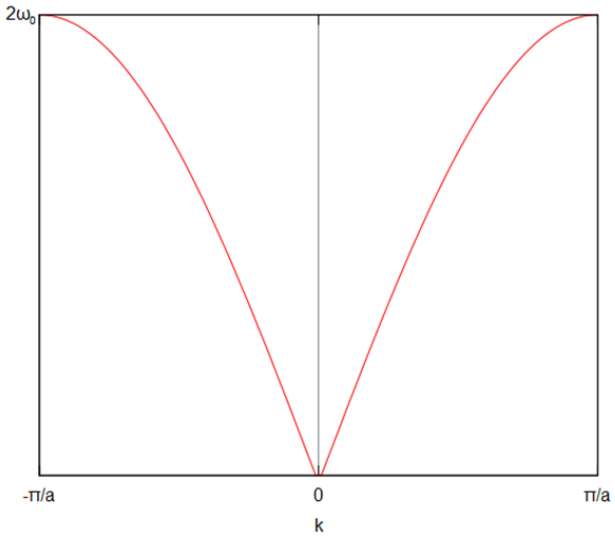

Fig. 4-2 Dispersion relation of LA phonon for the 1D atom chain model, and a is the spacing between each atoms.

In this thesis, the central frequency of excited acoustic waves is around ten to hundred GHz and its wavelength is around ten nanometer or more. The fact means that the wave vector is still located near the center of the Brillouin zone, i.e. the acoustic wavelength is greater than several atom spacing. So the continuum linear elastic theory is still reasonably available and thus adopted in the following calculation.

4.2 Acoustic Waves in Bulk Crystals

In a bulk crystalline solid, which is often taken as an infinite medium, the waves are characterized by plane waves with three different polarization types. Christoffel's equation and the slowness surfaces are useful to describe the velocities of (quasi-) longitudinal and (quasi-) transverse waves in any directions of space [4.4]. Fig. 4-3 shows the GaAs slowness surfaces in the (001) surface, in which it indicates the highly anisotropism and thus states the necessity of anisotropic waveguide model used in the following case.

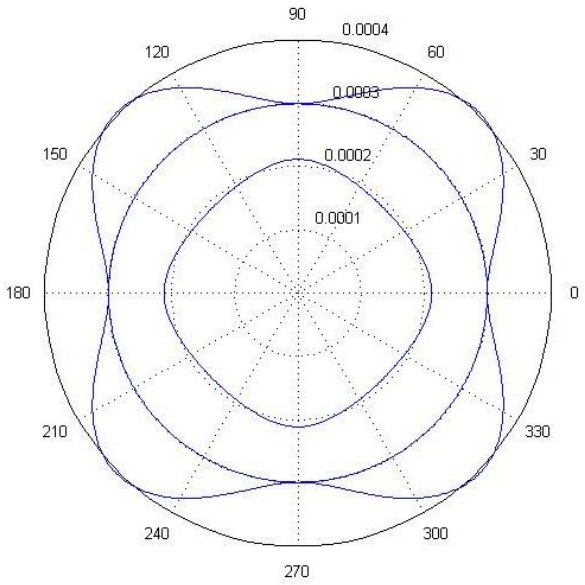

Fig. 4-3 GaAs (cubic system) slowness surfaces (unit: m^{-1}) in the (001) surface. In the [100] and [010] direction, the corresponding velocities of quasi-longitudinal and quasi-transverse is 4731m/s and 3347m/s, respectively.

4.3 Acoustic Waves in Finite Solid – Waveguide Theory

In a finite elastic object like a plate or a rod, acoustic waves would be reflected at the boundary. For satisfying the boundary conditions, the reflection of an oblique incident wave at the free surface must be accompanied with different wave type generated and reflected. For successive reflections at the surface, as shown in Fig. 4-4, it will totally form an overall lateral distribution and propagate toward the specific direction. This phenomenon leads to the idea of acoustic waveguides. Thus in the following, an isotropic and an anisotropic models will be introduced for qualitative elucidation of the phenomenon we observed experimentally.

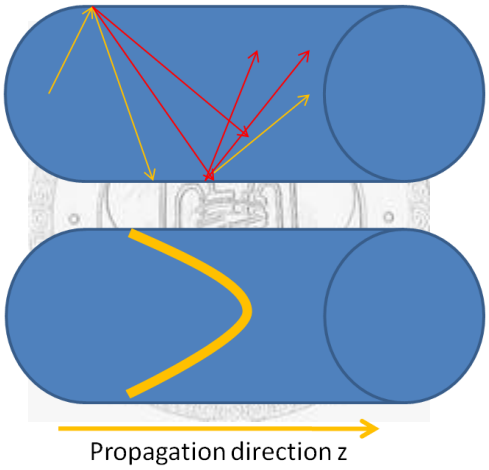

Fig. 4-4 (a) Schematic diagram of successive reflections of acoustic waves at the free boundary, in which different wave type are represented by different color. (b) Overall lateral distribution that propagates toward the z direction

4.4 Acoustic Guided Waves in an Isotropic Cylindrical Rod

The problem of elastic wave propagation in an isotropic infinite solid cylinder was first developed by Pochhammer in 1876 and Chree in 1889 independently. The problem was treated based on three-dimensional elasticity and the full theory describes the propagation of axisymmetric, torsional, and flexural waves. Being as start to the waveguide theory and for the comparison to anisotropic cases, we will give a brief

description of Pochhammer Chree theory in the following.

For isotropic material, the displacement can be derived from a scalar potential ϕ and a vector potential Ψ, so that

$$u = \nabla\phi + \nabla\times\Psi . \tag{4.1}$$

Because the vector identities $\nabla\cdot\nabla\times\Psi = 0$ and $\nabla\times\nabla\phi = 0$, these two potentials represent different physical meaning. Strains associated with dilatation, causing volume change, are expressed by ϕ, and shear strains, in the contrary, are expressed by Ψ. After substitution of these two potentials in the wave equation, we get

$$\begin{aligned} \nabla^2\phi - \frac{1}{V_L}\frac{\partial^2\phi}{\partial t^2} = 0 \\ \nabla^2\Psi - \frac{1}{V_T}\frac{\partial^2\Psi}{\partial t^2} = 0 \end{aligned}, \tag{4.2}$$

where $V_L = \sqrt{\frac{C_{11}}{\rho}}$ and $V_T = \sqrt{\frac{C_{44}}{\rho}}$ are the phase velocity of bulk longitudinal and transverse waves, respectively. After solving equation (4.2) with some reasonable assumptions [4.4], the vector potential and scalar potential solution are

$$\phi = AJ_n(pr)\cos(n\theta)e^{i(\omega t - kz)}, \tag{4.3}$$

$$\Psi_z = BJ_n(qr)\cos(n\theta)e^{i(\omega t - kz)},$$

$$\Psi_r = \psi_r(r)\sin(n\theta)e^{i(\omega t - kz)},$$

$$\Psi_\theta = \psi_\theta\cos(n\theta)e^{i(\omega t - kz)}.$$

The equation of displacement field is obtained by substituting equation (4.3) into equation (4.2), and thus also strain and stress field can be solved as long as the displacement is known. According to the order in azimuthally direction, the normal modes can be grouped into three families: (1) compressional waves, which is axially

symmetric with the displacement u_r and u_z independent of θ; (2) torsional waves with u_θ independent of θ ; and (3) flexural waves with u_r, u_θ, and u_z dependent on r, θ, and z. To derive Pochhammer Chree equation, the only type of waves we focus on are the compressional waves, its radial and axial components of displacement become

$$\begin{aligned} u_r &= -[pAJ_1(pr) + ikCJ_1(qr)]e^{i(\omega t - kz)} \\ u_z &= -[ikAJ_0(pr) + qCJ_0(qr)]e^{i(\omega t - kz)} \end{aligned}, \tag{4.4}$$

where $p = [(\frac{\omega}{V_L})^2 - k^2]^{\frac{1}{2}}$, and $q = [(\frac{\omega}{V_T})^2 - k^2]^{\frac{1}{2}}$. By setting the stress T_{rr} and T_{rz} to be zero at the surface,

$$\begin{aligned} T_{rr} &= \lambda S + 2\mu \left.\frac{\partial u_r}{\partial r}\right|_{r=a} = 0, \\ T_{rz} &= \mu(\frac{\partial u_r}{\partial z} + \left.\frac{\partial u_z}{\partial r}\right|_{r=a}) = 0, \end{aligned} \tag{4.5}$$

where λ and μ are Lame constants, which are related to stiffness constants and used here for more simple expression, and S is the divergence of displacement($S = \nabla \cdot u$). For non-trivial solutions, the determinant need to be zero, so we can obtain:

$$\frac{2p}{a}(q^2 + k^2)J_1(pa)J_1(qa) - (q^2 - k^2)^2 J_0(pa)J_1(qa) - 4k^2 pqJ_1(pa)J_0(qa) = 0 . \tag{4.6}$$

This formula is the well-known Pochammer Chree equation. It contains the angular frequency ω and wavenumber k in the z direction (axial direction of rod), the velocity of bulk longitudinal and transverse waves, and the cylinder radius a. It gives the dispersion relation and mode pattern of the axisymmetric waves that are allowed to propagate in a cylindrical waveguide. In the next section, we will use the isotropic standard case as a special one to examine the validity of our anisotropic model which

should give the same results as Pochhammer Chree theory.

4.5 Acoustic Guided Waves in an Anisotropic Cylinder Waveguide

Acoustic guided waves in a homogenous anisotropic cylinder have been investigated by many methods. Because of its complexity, the problem was reduced to a special case of orthotropic cylinder by Mirsky [4.6] who is the first to study the axisymmetric wave propagation in a free, homogenous and infinite orthotropic cylinder based on the three-dimensional elasticity theory by using Frobenius series method. The orthotropic cylinder case was further extended to more complicated cases for different semi-analytical method. The cases includes composite cylinders, hollow cylinders (shells) or the one immersed under a liquid.

On the other sides, with the great progress in the computational capability, using numerical approaches like finite element method (FEM) [4.7], or semi-analytical finite element method (SAFE) [4.8] which reduced the problem to bi-dimensional case, i.e. only the cross-section is meshed by using finite element, had attracted some attention because of its ability to simulate waves propagation and analyze dispersion relation of non-cylindrical and fully anisotropic waveguide. Despite the great advantages of FEM and SAFE, the methods are quite complicate and lengthy in code writing.

However, for the vibration of a finite elastic object, Migliori and Visscher [4.9][4.10] used simple basis function for the variational method that led to an accurate and extremely flexible approach to compute the elastic resonance of a free and anisotropic elastic body of arbitrary shapes. The method is often called “Resonant Ultrasound Spectroscopy” (RUS) and is used in designed resonance experiments to obtain the

elastic constants by measuring the resonance frequencies of the elastic objects or vice versa [4.9]. Nishiguchi et al. [4.11] firstly used the RUS method to compute the acoustic phonon dispersion relation in rectangular quantum wires and classify the normal modes into four types including dilatational, shear, torsion and flexural modes based on the parity of phonon displacement field.

For its simplicity, in this thesis, the theoretical approach to an anisotropic waveguide is used as the same as that Nishiguchi developed. In the following, we will give the detailed description of RUS method which is based on variation method, and show the result of dispersion curve and mode pattern of displacement field.

4.5.1 Variation Method

By using the variational principle, the Lagrangian of a free 3D elastic object can be written in terms of displacements u_i and angular frequency ω:

$$L = \int_V [\frac{\rho}{2}\omega^2 u_i u_i - \frac{1}{2} C_{ijkl} u_{k,l} u_{i,j}] dV , \tag{4.7}$$

where ρ, C_{ijkl} and V is the mass density, the stiffness tensor and total volume of the rod, respectively. The basis functions, expressed by Φ_λ which comprise a complete set [4.12], are used to expand the displacement field:

$$u_i = \chi_{i\lambda} \Phi_\lambda . \tag{4.8}$$

Therefore equation (4.7) can be written as

$$L = \frac{1}{2}[\chi_{i\lambda}\chi_{i\lambda'}\rho\omega^2 \int_V \Phi^*_\lambda \Phi_{\lambda'} dV - \chi_{k\lambda}\chi_{i\lambda'} C_{ijkl} \int_V \Phi^*_{\lambda,l} \Phi_{\lambda',j} dV] . \tag{4.9}$$

It can be expressed in the much simpler form by matrix expression,

$$L = \frac{1}{2}[\omega^2 \chi^T E \chi - \chi^T \Gamma \chi] . \tag{4.10}$$

The matrix elements in E and Γ are defined:

$$E_{i\lambda';j\lambda} = \delta_{i,j} \frac{\rho}{V} \int_V \Phi^*_{\lambda'} \Phi_\lambda dV \,, \tag{4.11}$$

$$\Gamma_{i\lambda';l\lambda} = \frac{C_{ijkl}}{V} \int_V \Phi^*_{\lambda',j} \Phi_{\lambda,k} dV \,. \tag{4.12}$$

The derivative of L with respect to every expanded coefficient is set to be zero for requiring L to be an extremum ($\delta L = 0$), which reduced the problem to an eigenvalue problem,

$$[\omega^2 E - \Gamma]\chi = 0 \tag{4.13}$$

The solved eigenvalues and eigenvectors are corresponding to the normal mode frequencies and the mode displacement distribution respectively. Thus, for a specific wavenumber k , we can obtain corresponding frequency of each normal mode by using MATLAB code to calculate the matrix elements and solve its eigenvalues.

4.5.2 Basis Function

Because it is important to find an explicit form for the matrix elements of $E_{i\lambda';j\lambda}$ and $\Gamma_{i\lambda';l\lambda}$, the basis functions are chosen according to the shape of the sample. For parallelepipeds, a convenient choice is Legendre polynomial [4.12], while a series of expansion of power of x , y and z are suitable for a variety of shapes. Thus the basis functions used here are

$$\Phi_\alpha = \left(\frac{x}{r}\right)^p \left(\frac{y}{r}\right)^q e^{ikz} \,, \tag{4.14}$$

where α is the index of the assemble of (p,q) , and k is the wave vector along the z direction. The basis functions assumed here indicate that the normal modes with a certain mode pattern in the lateral x, y distribution are propagating along the z

direction of the cylindrical rod. However, being a semi-numerical approach, the number of basis function used is needed to be truncated at a given number l, so the condition given by $p+q \le l$ is verified [4.12]. By substituting the equation (4.14) into the equation (4.11) and yielding the matrix elements as

$$E_{i\lambda';j\lambda} = \delta_{i,j}\rho F(p+p';q+q'), \tag{4.15}$$

where the function F deals with the integration between each basis function. Since the functions are the combination of simple polynomials, an analytic result of the integration can be easily found, which make huge advantage in code writing,

$$\begin{aligned} F(p,q) &= \int_V (\frac{x}{r})^p (\frac{y}{r})^q dxdydz \quad = \int_{-\Delta}^{\Delta}\int_{-r}^{r}\int_{-\sqrt{r^2-y^2}}^{\sqrt{r^2-y^2}} (\frac{x}{r})^p (\frac{y}{r})^q dxdydz \\ &= 2\Delta \frac{(p-1)!!(q-1)!!}{(p-q-2)!!} \end{aligned} \tag{4.16}$$

Also the matrix elements $\Gamma_{i\lambda';l\lambda} = \frac{C_{ijkl}}{V}\int_V \Phi^*_{\lambda',j}\Phi_{\lambda,k}dV$: (4.17)

$$\Gamma_{1\lambda';1\lambda} = \frac{1}{r^2}C_{11}mm'F(m+m'-2;n+n') + \frac{1}{r^2}C_{44}nn'F(m+m';n+n'-2) + C_{44}q^2F(m+m';n+n')$$

$$\Gamma_{1\lambda';2\lambda} = \frac{1}{r^2}(C_{12}m'n + C_{44}mn')F(m+m'-1;n+n'-1)$$

$$\Gamma_{1\lambda';3\lambda} = \frac{-i}{r}q(C_{44}m - C_{12}m')F(m+m'-1;n+n')$$

$$\Gamma_{2\lambda';1\lambda} = \frac{1}{r^2}(C_{44}m'n + C_{12}mn')F(m+m'-1;n+n'-1)$$

$$\Gamma_{2\lambda';2\lambda} = \frac{1}{r^2}C_{44}mm'F(m+m'-2;n+n') + \frac{1}{r^2}C_{11}nn'F(m+m';n+n'-2) + C_{44}q^2F(m+m';n+n')$$

$$\Gamma_{2\lambda';3\lambda} = \frac{-i}{r}q(C_{44}n - C_{12}n')F(m+m';n+n'-1)$$

$$\Gamma_{3\lambda';1\lambda} = \frac{-i}{r}q(C_{12}m - C_{44}m')F(m+m'-1;n+n')$$

$$\Gamma_{3\lambda';2\lambda} = \frac{-i}{r}q(C_{12}n - C_{44}n')F(m+m';n+n'-1)$$

$$\Gamma_{3\lambda';3\lambda} = \frac{1}{r^2}C_{44}mm'F(m+m'-2;n+n') + \frac{1}{r^2}C_{44}nn'F(m+m';n+n'-2) + C_{11}q^2F(m+m';n+n')$$

4.5.3 Classification of Normal Modes

Another advantage of using a series of power of x, y, and z as basis functions is its simplicity for classification of normal modes. According to the parity of the displacement field, guided modes can be grouped into dilatational, torsional and flexural mode in a cylindrical waveguide. The classification is defined in Table 4-1. The parity is expressed by (μ,ν), where $\mu=(-1)^p$ and $\nu=(-1)^q$.

Table 4-1 Classification of normal modes

Classification	u_x	u_y	u_z
Dilatational	$(-,+)$	$(+,-)$	$(+,+)$
Torsion	$(-,-)$ $(+,+)$	$(+,+)$ $(-,-)$	$(+,-)$ $(-,+)$
Flexural	other	Other	other

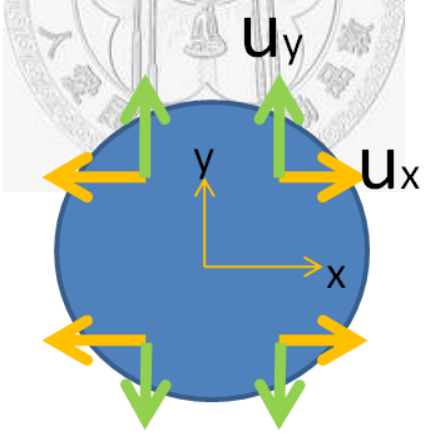

Fig. 4-5 Schematic diagram of the defined parity in displacement u_x and u_y of dilatational modes..

Based on the defined parity, the displacement components in x, y, z direction of dilatational normal modes are:

$$
\begin{aligned}
u_x &= \sum_{p,q=0}^{2(p+q)+1\le l} \chi_{1pq} (\frac{x}{r})^{2p+1} (\frac{y}{r})^{2q} e^{iqz} \\
u_y &= \sum_{p,q=0}^{2(p+q)+1\le l} \chi_{2pq} (\frac{x}{r})^{2p} (\frac{y}{r})^{2q+1} e^{iqz} \\
u_z &= \sum_{p,q=0}^{2(p+q)\le l} \chi_{3pq} (\frac{x}{r})^{2p} (\frac{y}{r})^{2q} e^{iqz}
\end{aligned}
\tag{4.18}
$$

4.5.4 Comparison with Pochhammer Chree Theory

As long as the elastic properties (stiffness constants and density) and the geometry (radius) are known, the RUS method can be used to find the dispersion relation. In this section, we use SiO_2 which is isotropic to test the anisotropic model – RUS method. For SiO_2, the stiffness constants are $: C_{11} = 78.5GPa$, $C_{12} = 16.1GPa$, $C_{44} = 31.2GPa$ and the density is $\rho = 2203kg/m^3$. Fig. 4-6 shows the dispersion relation from Pochhammer Chree theory and RUS method. It shows good agreement between two different approaches. However, there are extra modes by using RUS method with comparison to Pochhammer Chree theory. The reason is that one method uses the x, y parity while the other uses the r, θ parity to specify the normal modes. This reason will be confirmed later by comparing the displacement field of every normal mode.

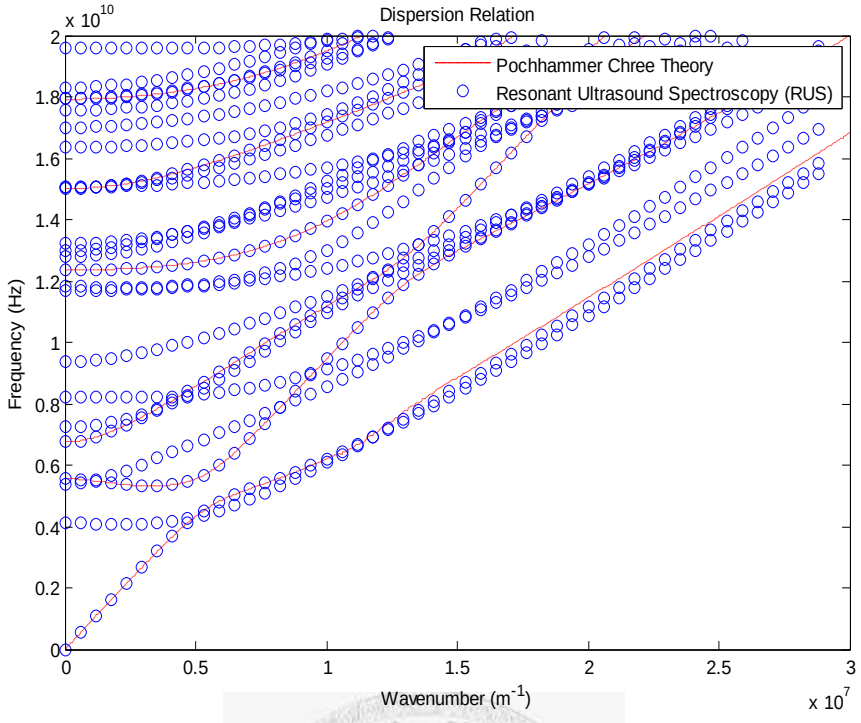

Fig. 4-6 Dispersion relation of a cylindrical waveguide of radius as 340nm and composed of SiO2. The red lines are from Pochhammer Chree theory, a standard solution for an isotropic waveguide. The blue circles are from RUS method.

The displacement fields of the first four modes are drawn in Fig. 4-7to Fig. 4-9. For the reason that even the same mode will show difference in mode pattern at different wave vector, and each mode will cross the other somewhere in the dispersion curve, we compare the mode pattern at a specific wave vector as $k = 0.25 \times 10^7 (m^{-1})$. The lowest mode, without cutoff frequency, shows the axisymmetric parity for both approaches. But the second mode in the RUS method shows absolutely different parity in x, y directions and thus excluded from the Pochhammer Chree Theory. Mode 3 of the RUS method (Mode 2 of the Pochhammer Chree theory) shows major components in the u_x, u_y rather than u_z. In addition, it should be noticed that as $k \to 0$ for this mode, the entire rod will exhibit pure vibration in the radial direction, and it is usually called "breathing mode", which is most commonly excited and observed in the previous

pump-probe studies of vibration response of nano-structures [4.13]. The displacement distribution of mode 4 shows the parity like mode 2 as well, thus not appearing in the Pochhammer Chree theory again.

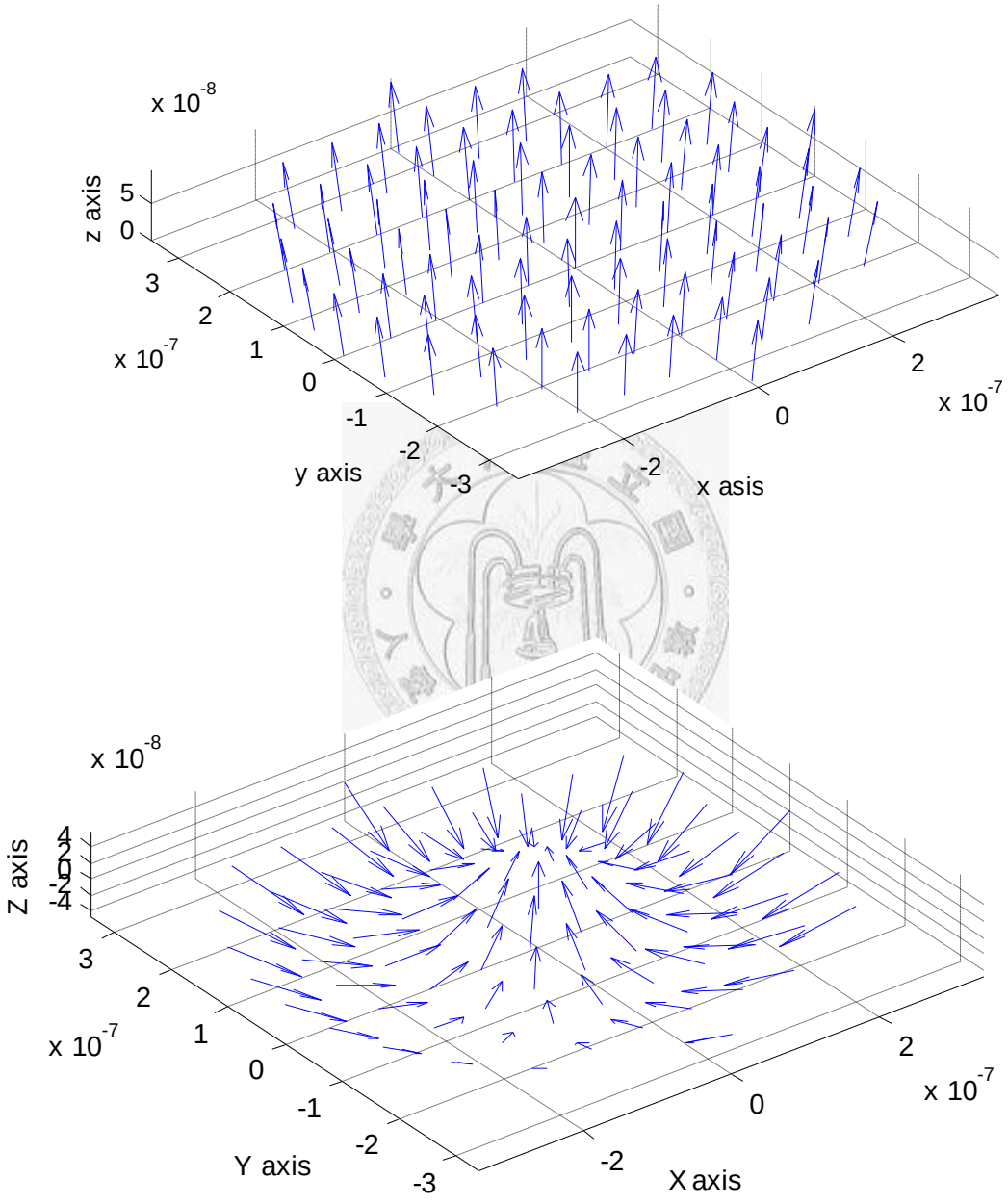

Fig. 4-7 Displacement fields of (a) mode 1 and (b) mode 2of Pochhammer Chree theory.

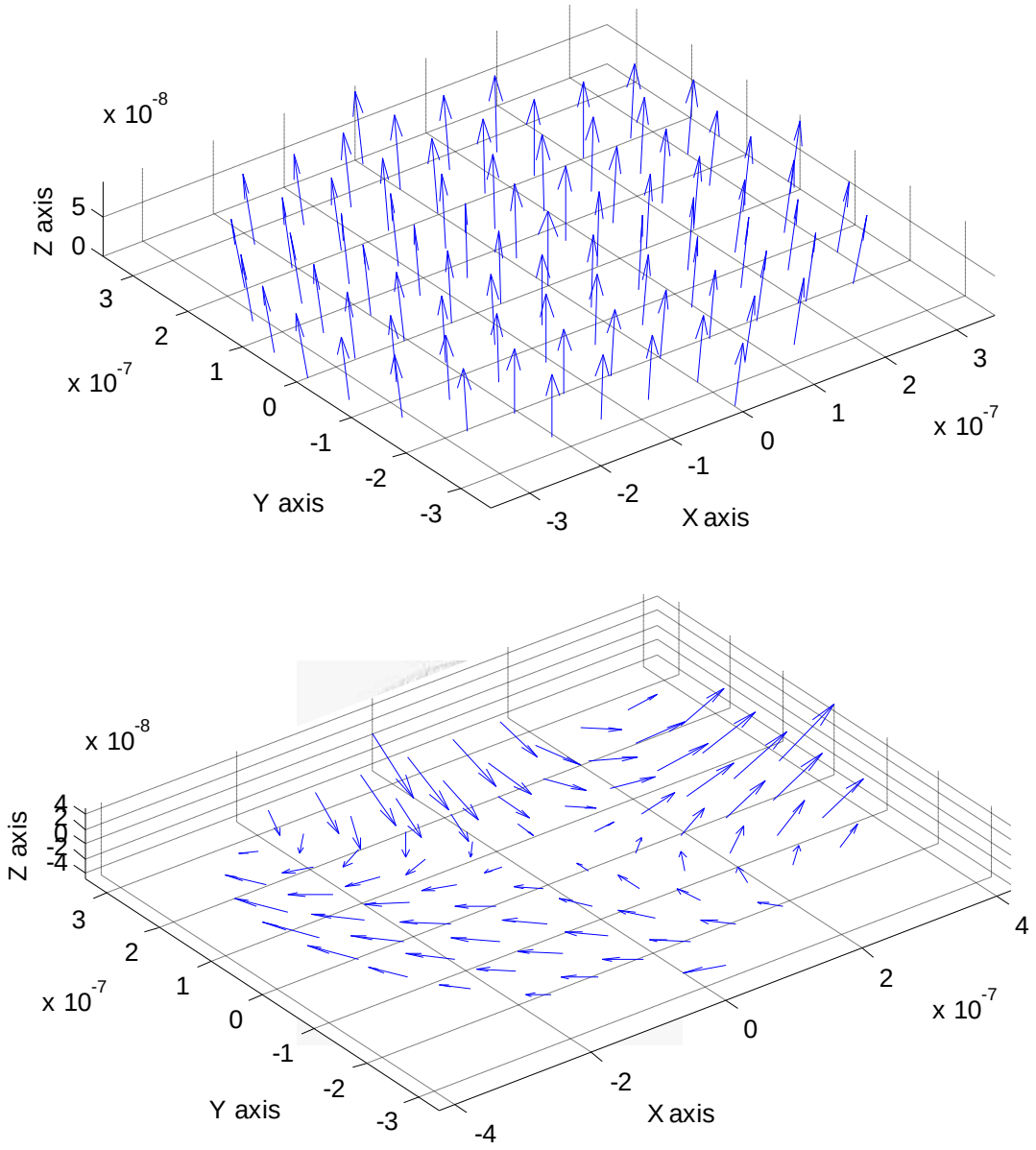

Fig. 4-8 Displacement fields of (a) mode 1 and (b) mode 2 of RUS method

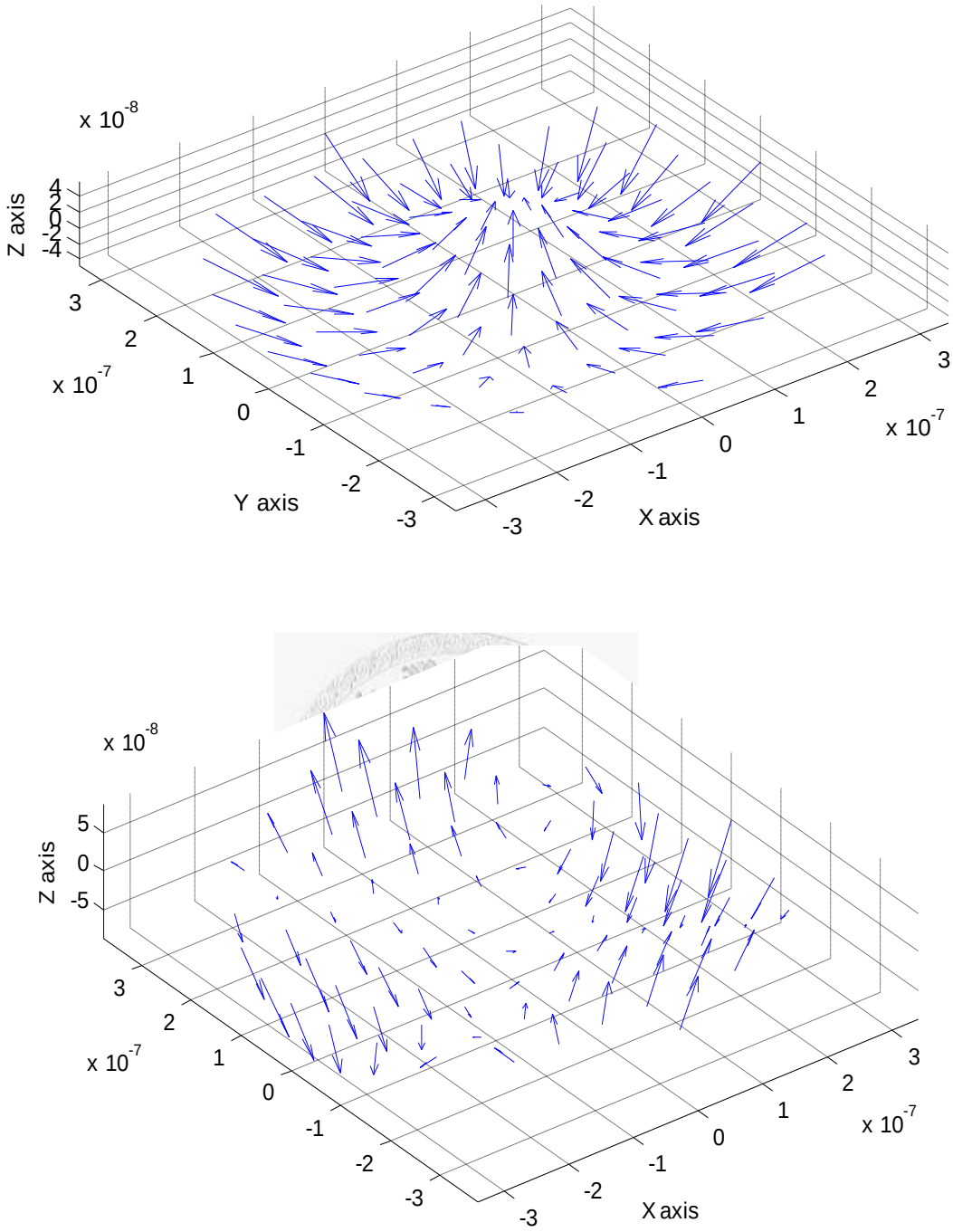

Fig. 4-9 Displacement fields of (a) mode 3 and (b) mode 4 of RUS method

4.5.5 Dispersion Curve and Mode Distribution of Guided Waves in GaAs NRs

In our experiment, the spot size of the focused pump beam is much greater than the diameter of nanorod, thus the assumption of dilatational acoustic waves excited by the homogenous expansion of gold nanodisk is reasonable so it is the only type we interested. The dispersion curve of dilatational modes of a 340nm-diameter GaAs nanorod is given in Fig. 4-10 and compared with the isotropic model assuming uniform velocity of the longitudinal and the transverse are 4731 m/s and 3347m/s, which are the typical velocities in the (100) direction. According to the waveguide theory, it is worthy to note there are discrete modes with certain mode pattern that can propagate inside a nanorod. This is because of the confinement of the boundary, the allowed modes and its phase velocity as well as group velocity is very different from the case of a bulk crystal which can be easily described by plane waves with longitudinal and transverse velocities.

The actual displacement field of excited guided modes will be given in the later chapter for discussion. However, it can be found that the distribution of displacement field of the first four modes of anisotropic case is nearly the same as the isotropic one at low wavenumber region; however, significant difference in dispersion relation at higher wavenumber region will make the mode pattern more complicate and different.

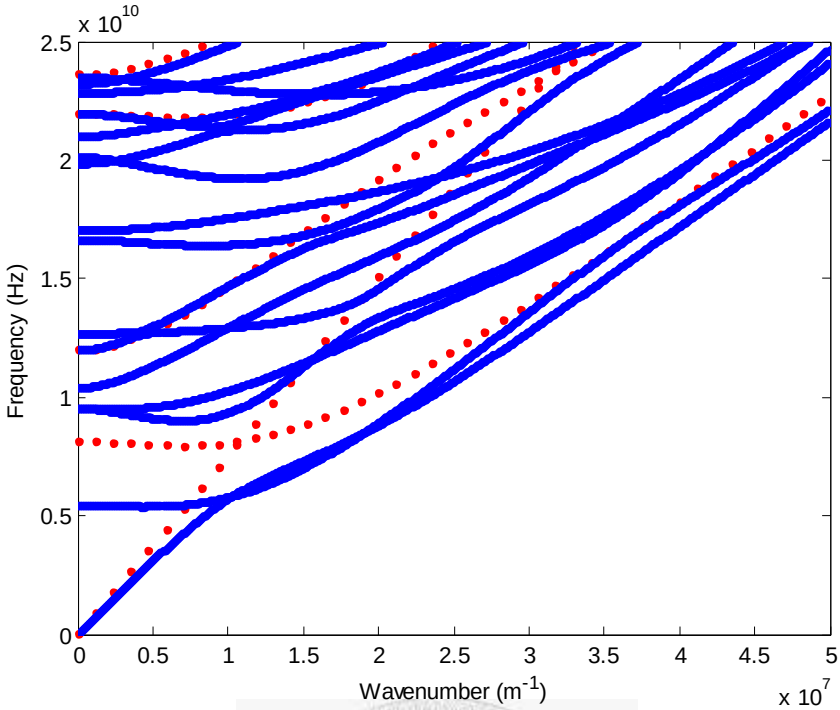

Fig. 4-10 Calculated dispersion relations of a 340nm-diameter GaAs nanorod. The red dot is calculated from Pochhammer Chree equation, and the solid blue line is calculated from RUS method.

Reference

[4.1] C. Kittel, *Introduction to Solid State Physics*. 8th edition. New York: Wiley (2005).

[4.2] Sebastain G. Volz and G. Chen, "Molecular dynamics simulation of thermal conductivity of silicon nanowires," *Appl. Phys. Lett.*, **75**, 2056 (1999).

[4.3] S.J.A. Koh, H.P. Lee, C. Lu and Q.H. Cheng, "Molecular dynamics simulation of a solid platinum nanowire under uniaxial tensile strain: Temperature and strain rate effects," *Phys. Rev. B.*, **72**, 085414 (2005).

[4.4] E. Dieulesaint and D. Royer, *Elastic waves in solids*. Springer, (1995).

[4.5] Anthony D. Puckeet, M.L. Peterson, "A semi-analytical model for predicting multiple propagating axially symmetric modes in cylindrical waveguides," *Ultrasonic*, **43**, 197 (2005).

[4.6] Mirsky. "Axisymmeteric vibration of orthotropic cylinders," *J. Acoust. Soc. Am.* **36**, 2106 (1964).

[4.7] A.-C. Hladky-Hennion. "Finite element analysis of the propagation of acoustic waves in waveguides," *J. Sound. Vib.* **194**(2), 119 (1996).

[4.8] Marzani, E. Viola, I. Bartoli, F.L. di Scalea, P. Rizzo. "A semi-analytical finite element formulation for modeling stress wave propagation in axisymmeteric damped waveguided." *J. Sound. Vib.* **318**, 488 (2006).

[4.9] Migliori, J.L. Sarrao, William M. Visscher, T.M. Bell, Ming Lei, Z. Fisk and R.G. Leisure. "Resonant ultrasound spectroscopic techniques for measurement of the elastic moduli od solids." *Physica B.* **183**, 1 (1993)

[4.10] William M. Visscher, A. Migliori, T. M. Bell, and R.A. Reinert. "On the normal modes of free vibration oh inhomogeneous and anisotropic elastic objects." *J. Acous. Soc. Am.*, **90**(4), 2154 (1991).

[4.11] N. Nishiguchi, Y. Ando and M. N. Wybourne. “Acoustic phonon modes of retangular quantum wires.” *J. Phys.: Condens. Matter.* **9**, 5751-5764 (1997).

[4.12] R.G. Leisure and F.A. Willis. “Resonant ultrasound spectroscopy.” *J. Phys.: Condens. Matter,* **9**, 6001-6029 (1997).

[4.13] M. Hu, X. Wang, G. Hartland, P. Mulvaney, J. Juste, and J. Saders, “Vibrational response of nanorods to ultrafast laser induced heating: Theoretical and experimental analysis.” *J. Am. Chem. Soc*, **125**, 14925 (2003).

Chapter 5 Experimental Results and Discussion

5.1 Experiment Results (probe 880nm, pump 440nm)

As we mentioned in chapter 2, two-color pump-probe scheme was used for a much better signal-to-noise ratio (SNR). Since the modulation of optical constants perturbed by the acoustic disturbance is more effective near the band gap of GaAs ($E_g = 1.43eV$, 873nm), the probe wavelength was first chosen to be 880nm (from mode-locked Ti-sapphire laser) and thus the pump wavelength was 440nm (frequency doubled from Ti-sapphire laser).

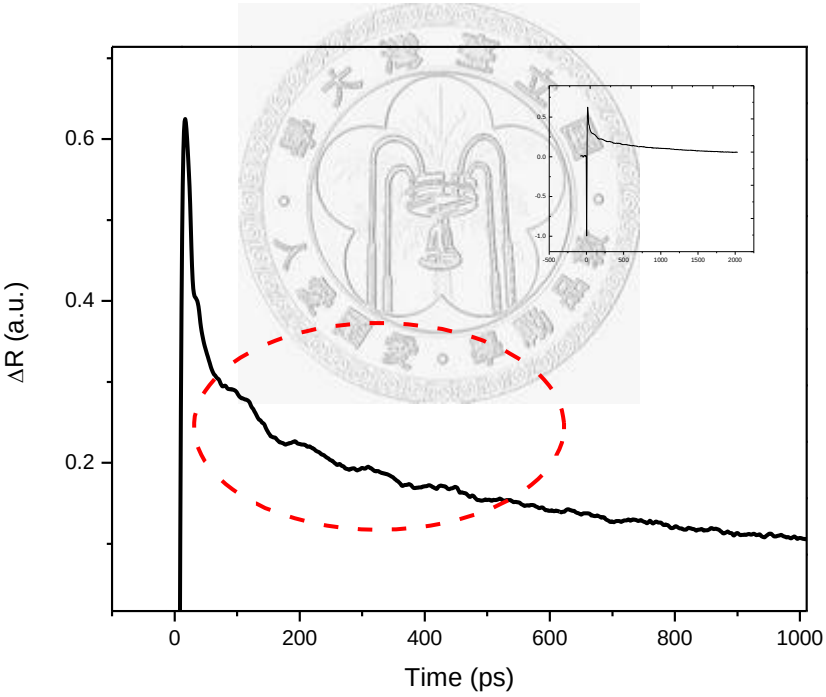

Fig. 5-1 Transient change in reflectivity of the sample induced by the pump beam (880nm). A small oscillatory signal that is attributed to coherent phonon generation of the sample is highlighted in the figure. The inset shows the full measured trace.

The inset of Fig. 5-1 shows the typical transient reflectivity change of pump-probe measurement of Au-attached GaAs nanorods. We divided the signals into two parts: (1) the carrier dynamic, which lead to the main character of the signal, i.e. the sharp change

and the following rapid exponential decay. The sharp change is induced by the arrival of pump pulse which excites sample's electronic configuration and thus perturbs the reflectivity of the following probe. After the excitation, the electronic configuration would rapidly release the excess energy and return to steady state, and this lead to the following exponential decay character.

However, carrier dynamics studies in the designed samples about size and optical wavelength dependencies are beyond this thesis scope so the comparison and the discussion about the difference of this main character of the signal are ignored. The only thing we interested is the second part: damped oscillations, which are highlighted in Fig. 5-1, accompanying with the carrier dynamic response after the excitation, and it is attributed to the modulation due to coherent phonon generation.

For the purpose of studying the characters of acoustic responses of Au-attached GaAs nanorods, we first fitted the function of exponential decay to remove carrier dynamic background. The frequencies of acoustic responses were identified by performing fast Fourier transform (FFT) to the oscillatory signals. The background-subtraction oscillations and the frequency spectra of 340nm-diameter samples are shown in Fig. 5-2. Since the frequency peaks that below the noise level is meaningless, and the possible artifacts which may result from the fitting and FFT procedures (the picket-fence effect and the leakage effect), we only discussed the most dominating frequency. In the 340nm-diameter case, the frequency is around 9.3GHz. In other cases of smaller diameter, the measured frequencies show dependency on the diameter. Here, according to the possible acoustic dynamic response as we discussed in Chapter 3, we can reasonably conclude that the frequency was contributed from the radial breathing mode vibration of individual GaAs nanorod. The interpretation can be supported by the following arguments.

Based on the previous investigation done by Yi-Hsin Chen (a former member of our group) in which he showed that for the samples with Au attached and without Au attached the dominating frequencies are almost the same under this pump-probe wavelength setup (probe: 880nm, pump: 440nm). In spite of the elastic anisotropism of GaAs, both results are in good agreement with the predicted breathing mode frequency of simplified isotropic theory. Second, by analyzing the phase of oscillation, the signals in both cases behave like cosinusoidal oscillation, i.e. the phase is around 0° at time zero. The phase was believed to be one of the characters of the signal from structure vibration for a step-like excitation [5.1].

To further confirm the validity of this conclusion, the size dependency was compared to formula (2.1), where V_L is 4731m/s, the typical longitudinal velocity in [001] direction, and the parameter τ is 2.14 for Poisson ratio used is 0.312. As shown in Fig. 5-3, the frequencies show the inverse proportionality to the diameter, and this is a typical character for radial vibration, i.e. the smaller object has the higher vibration frequencies. All the measured results exhibit good agreement to the breathing mode theory.

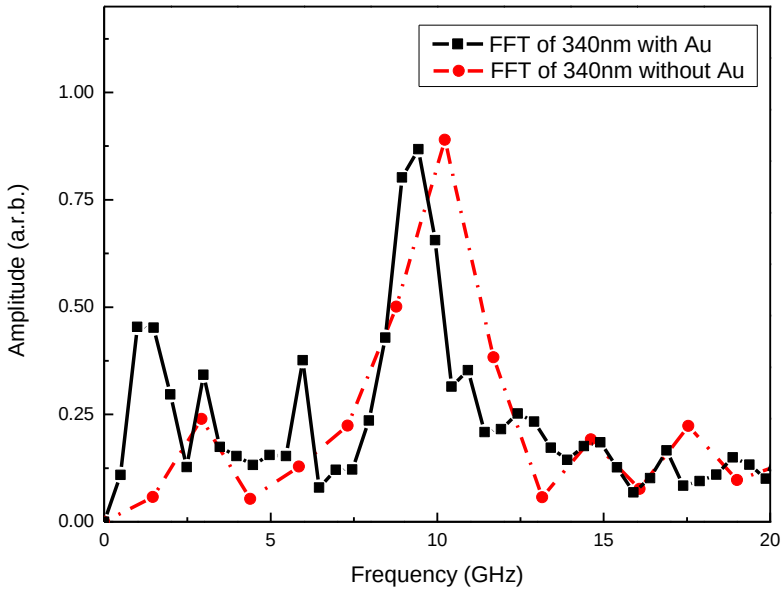

Fig. 5-2 Frequency spectra of 340nm-diameter nanorod samples. (black line: the sample with Au attached, red line: without Au attached)

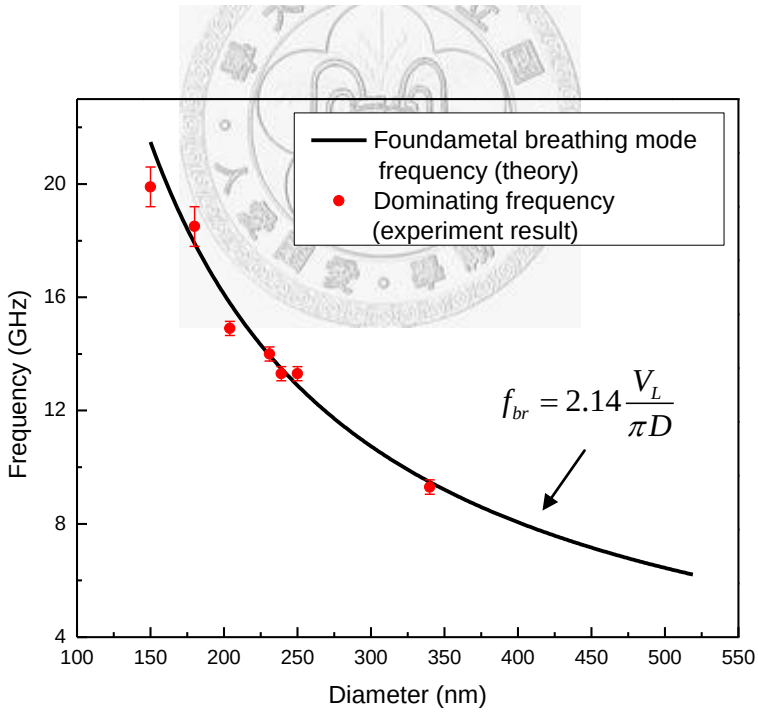

Fig. 5-3 Size dependency of the dominating frequency under 880nm probe used

5.2 Experimental Result (probe 1120nm, pump 390nm)

Although in the former scheme (probe 880nm, pump 440nm) the signal of breathing vibration of individual rod is dominating and overwhelming, the other acoustic dynamic responses may play a role for different probe wavelength since the detection mechanism of the each response depends on the probing optical wavelength, such as backward Brillouin oscillations and surface acoustic waves (SAWs). So in this section, we changed the probe wavelength from near infrared (880nm) to infrared (1120nm) region to study the acoustic responses of the structure. The wavelength was settled on 1120nm due to the power optimization for the OPO that was pumped by 780nm pulses which are the strongest power output from the Ti-sapphire laser. Here, although the pump wavelength is different (440nm vs. 390nm), the excitation can be still regarded as equivalent under these two schemes due to the same optical response of Au and GaAs in this ultraviolet regime.

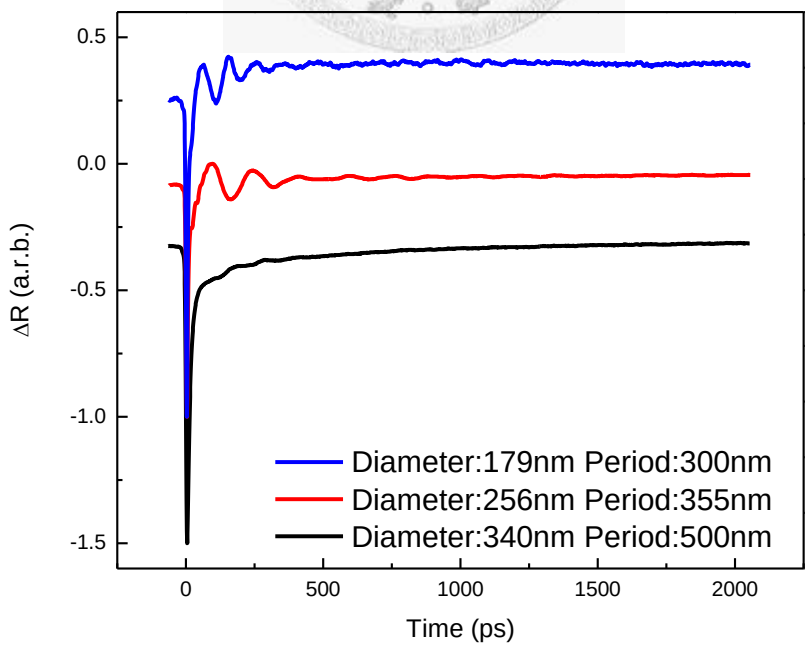

Fig. 5-4 Transient reflectivity change traces of different sample of different diameter and period under 1120nm probe used

Fig. 5-4 shows the experimental results for three different size cases under the infrared probe: (1)340nm diameter (period 500nm) (2) 256nm diameter (period 355nm) and (3) 179nm diameter (period 355nm). All of these samples are with around 720nm height.

Similarly, we neglected the difference of carrier dynamics and mainly focused to the damped oscillations observed. As one can see, there are many interesting and surprising things under this scheme: first, relatively huge oscillatory signal detected in small-diameter cases (< ~300nm) for 1120nm probe used. The amplitude of the oscillatory signal is quite different as compared to the results of near infrared probe (880nm). Fig. 5-5 shows the comparison between the results of two different probe wavelength but of identical sample (diameter: 231nm), one can easily observe that the sensitivity of detected oscillatory signal of these two are very different (although the carrier dynamic is different).

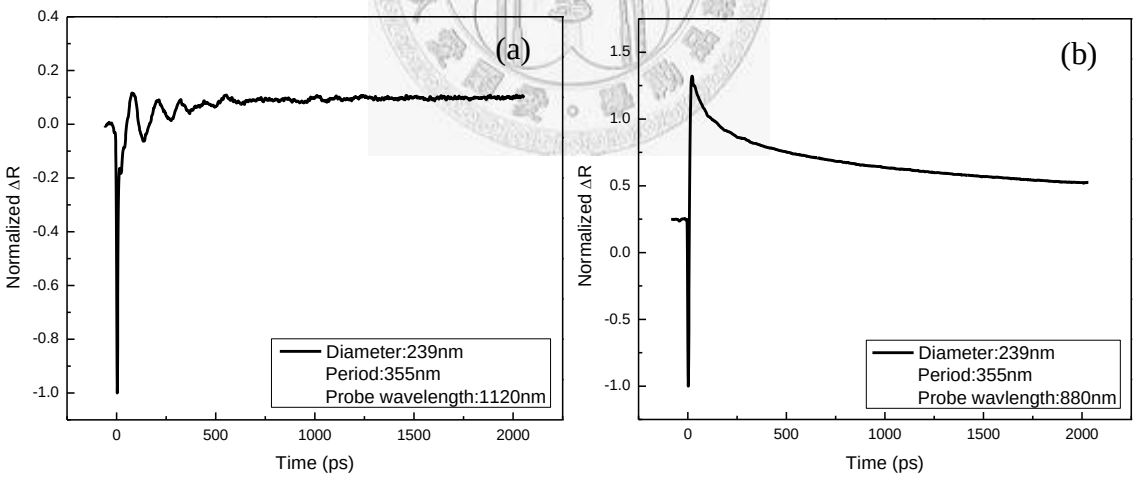

Fig. 5-5 Transient reflectivity change of the sample of 239nm-diameter and 355nm-period for (a) infrared (1120nm) probe and (b) near-infrared (880nm) probe. (each trace was normalized by its minimum value)

In order to analyze the frequencies, data approach for fitting to remove the background and FFT for frequency identification were used as before. Fig. 5-6 shows two data of the background-subtraction oscillations in time domain, and it should be

noted as the second interesting things that there are echo-like signals at a later point in time. These phenomena observed are quite different to those observed in that of 880nm probe used. In Fig. 5-6, the overall signal can be roughly identified that there is discontinuity of the oscillation at around 400~500ps, and thus we try to divided the oscillatory signal into two parts: (1) the initial oscillations and (2) the echo-like oscillations.

In the following, we divide the signal analysis and discussion to that in frequency domain and time domain.

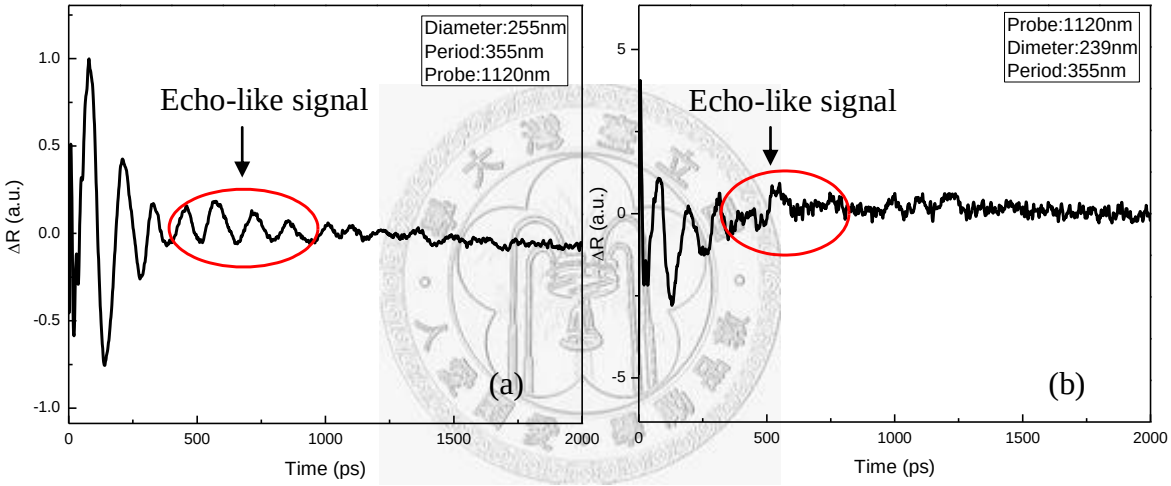

Fig. 5-6 (a) Background-substration oscillatory signal of the sample of 256nm diameter and 355nm period. (b) The signal of the sample of 239nm-diameter and 355nm-period.

5.2.1 Frequency Domain Analysis

Since the appearance of the echo-like signals states the possibility that different types of oscillations may occur at different timeframe, FFT was employed to the different parts of overall oscillatory signal. One was chosen for all the recorded time (around 2000ps), which possess the better resolution in the frequency domain, another was chosen for the initial oscillations, and the other was chosen to the echo-like oscillations. From Fig. 5-7, it is clear that dominating frequency at different time are nearly the same. It means that the oscillations of proceeding one and the later one come from the same physical mechanism. This fact strikes out the possibility of different probe sensitivity in the rod and substrate region which make the detected signal appear once again when acoustic waves traveling into the substrate [5.2].

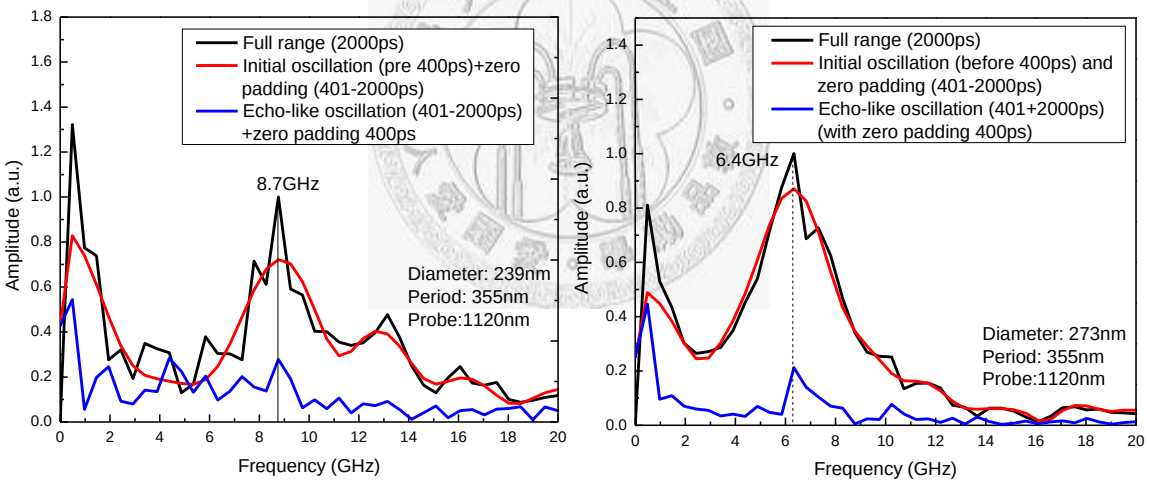

Fig. 5-7 Frequency spectra of the signal at different timeframe: Black line is full oscillatory signal, red line is that of initial oscillation, and blue line is that of echo signal. (a) The signal of the sample of 239nm diameter and 355nm period. (b) The signal of the sample of 273nm diameter and 355nm period. Note: Zero padding was used to make the length of each data equal to fairly compare

However, it is most important and surprising that the dominating oscillatory signal here is not the breathing mode of GaAs nanorods since the frequencies are absolutely different to those of 880nm probe used. Fig. 5-8 and Fig. 5-9 show the frequency spectra of identical samples but under near infrared (880nm) and infrared (1120nm)

probe. The frequencies observed are absolutely different for different probe in these cases. (One would expect that frequency of vibration modes are unrelated to the optical probing wavelength used).

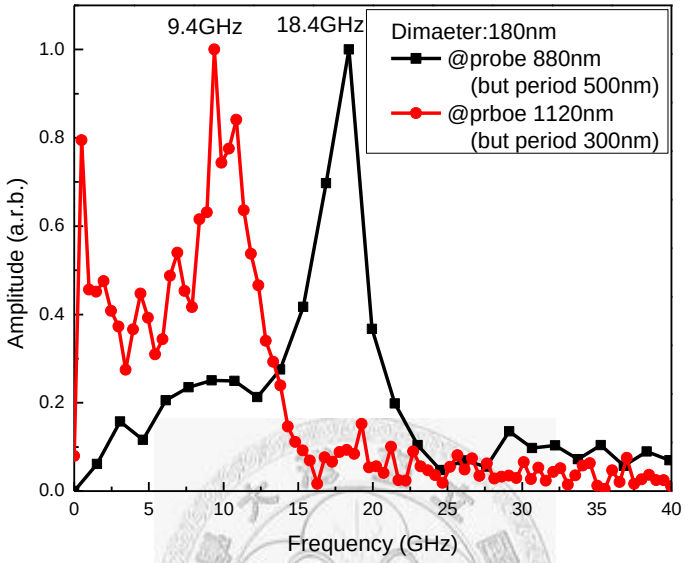

Fig. 5-8 Frequency spectra of the signal of the sample of 180nm diameter for 880nm probe (black-square line) and 1120nm probe (red-circle line). The dominating peak in red-circle line represents the radial breathing mode of GaAs nanorods.

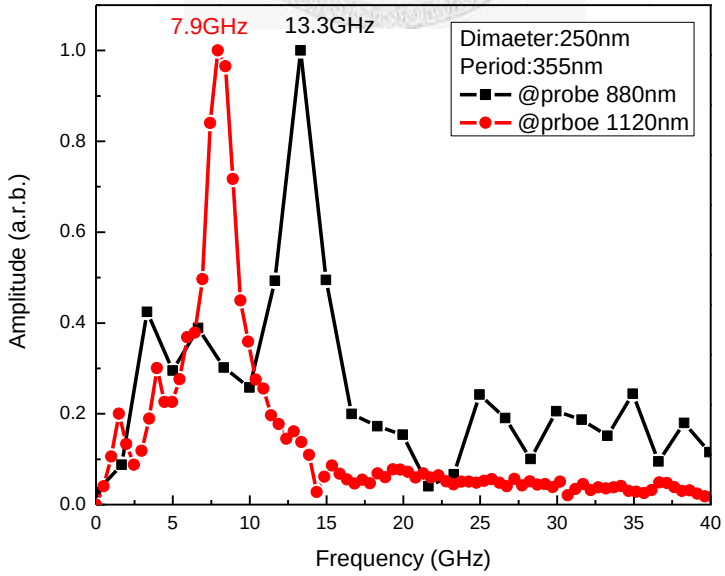

Fig. 5-9 Frequency spectra of the signal of the sample of 250nm diameter for each 880nm probe (black-square line) and 1120nm probe (red-circle line). The dominating peak in red-circle line represents the radial breathing mode of GaAs nanorods.

We conducted a size-dependency experiment by testing a series of different samples. Similarly, the frequencies measured show the diameter dependency. Therefore, it also reveals that the signal should be another vibration modes of the structure but not the breathing mode of GaAs nanorods. The frequency versus the rod diameter under the infrared probe (1120nm) is shown in Fig. 5-10. The blue line is the predicted breathing mode frequency as we stated in previous chapter. The red line represents the lateral vibration of a free Au nanodisk. In the figure, the measured dominating frequencies match the red line (lateral vibration of a free Au nanodisk) much better than the blue line (breathing mode of GaAs nanorods). A slight discrepancy between the red line and the measured results should result from the boundary condition assumption. In reality, since the Au is deposited on the GaAs nanorod, the free boundary condition assumed somehow is not valid. The vibration frequency would become higher because of boundary effect. The experimental results are in agreement with the predicted trend.

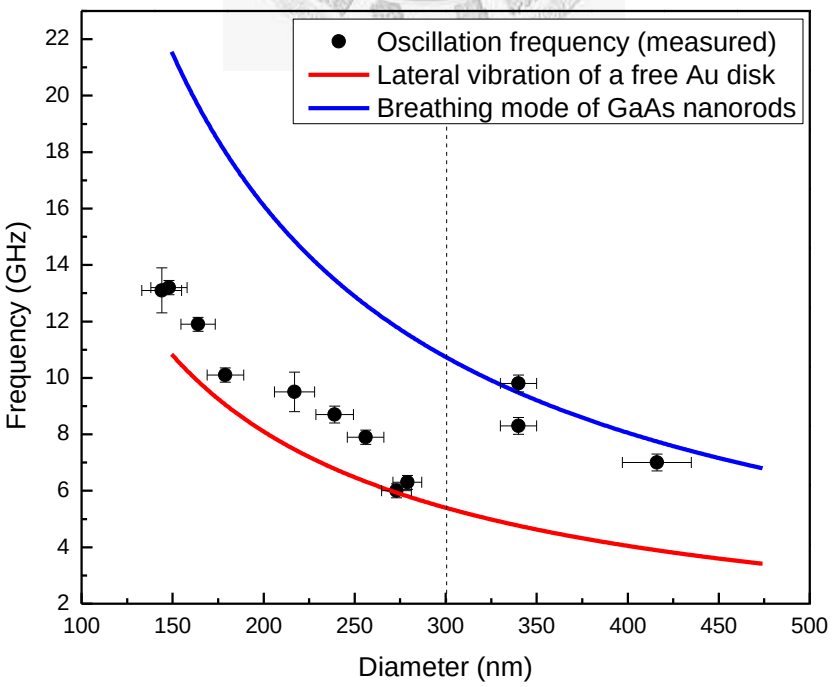

Fig. 5-10 Dominating frequency versus the diameter of the rod under 1120nm probe.

Therefore we suggested that the signal is induced by the vibration of the Au nanodisk for infrared probe (1120nm). There are more arguments to further support the above statement: a high frequency signal with around 52GHz just after the time zero can be observed in this scheme, but it occurs nowhere in the cases of 880nm probe used. The fact is illustrated in Fig. 5-11. (The signal do occur in all the cases of small diameter (<300nm) under 1120nm probe.) Such a high frequency signal in our designed samples could only come from the thickness vibration of the gold nanodisk. By substituting the longitudinal velocity of 3240m/s in Au [5.3] into formula (2.5), the estimated thickness is around 30nm, which is roughly the same as the actual size of deposited Au nanodisk that is identified from the SEM image. (As shown in Fig. 5-12)

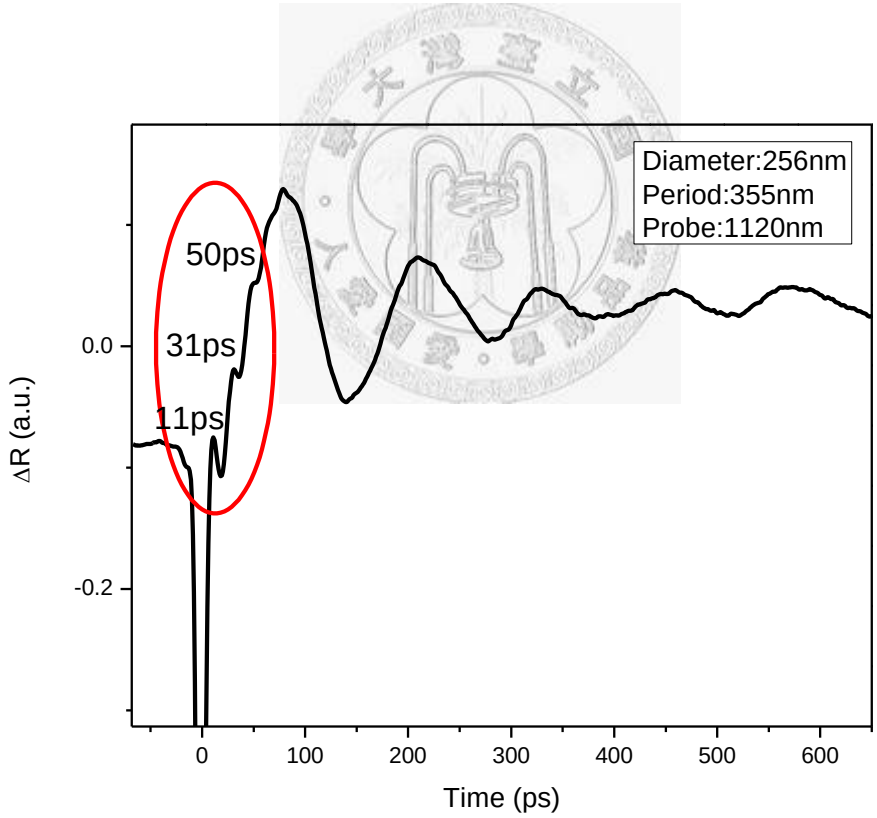

Fig. 5-11 The measured trace of transient change in reflectivity of the sample of 256nm diameter and 355nm period.(The frequency of the oscillation highlighted is around 52GHz)

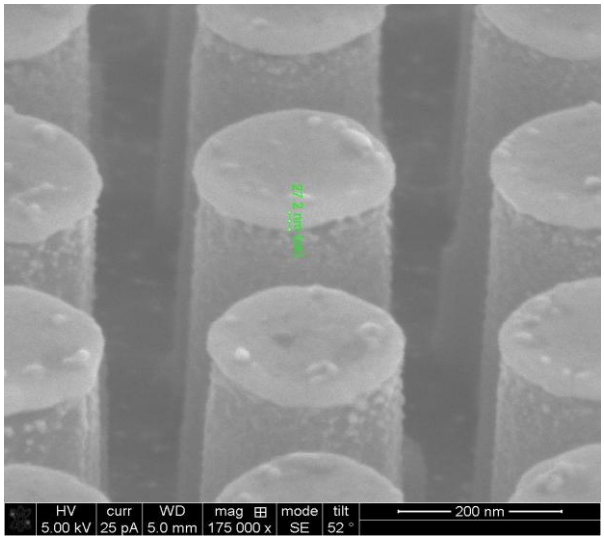

(a)

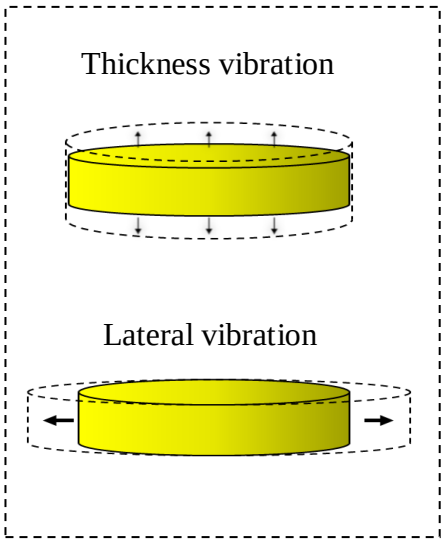

(b)

Fig. 5-12 (a) SEM image of the Au-attached GaAs nanorods. In this figure the thickness of metal layer can be identified as ~27nm. The graph is taken by Hung-Pin Chen who is a member of our group. (b) Schematic diagram of lateral and thickness vibration of a nanodisk.

These experimental results are in agreement with the intuition of the mechanical vibration: for a disk, a mostly possible mode excited by homogeneous thermal expansion is radial vibration rather than thickness vibration. This is because the expansion coordinates projects relative huge components on radial mode rather than the other. Another point is the nature that a mode with lower frequency are easily excited and survived. So the radial mode is the major one under this optical excitation is not surprising. By deducing from the above discussion, we concluded that not only thickness vibration but also the radial vibration (major one) are observed for infrared probe used, so it is quite reasonably to recognize the oscillatory signals are mainly induced by the Au nanodisk vibration.

However, for another cases of 340nm diameter and 440nm diameter, the signals observed return to that of breathing mode of GaAs nanorods, as shown in Fig. 5-10. Additionally, as shown in Fig. 5-4, the sensitivity of detected oscillatory signal is relative small as compared to the other cases for the infrared probe (1120nm). In fact,

the sensitivity of these two is more like those of 880nm probe used.

5.2.2 Detection Mechanism for the Infrared Probe (1120nm)

Now we have to figure out the problems about why different type of oscillatory signals dominate in two different probe wavelength schemes (for the samples of diameter < 300nm), and why the signal alters as the rod size is bigger than around 300nm (for the same probe of 1120nm)?

In fact, all of these phenomena discussed above reveal the implicit answer of the intervention of localized surface plasmon resonance (LSPR) occurred in the deposited Au nanodisks. As we mentioned in Chapter 3, by choosing a suitable optical wavelength, most of researchers made use of the LSPR effect to enhance the optical detection of acoustic modes in metal nanoparticles. That is because the resonance frequency of collective electrons in metal nanoparticles is highly sensitive to geometry and the environment surrounded. Acoustic modes permit a way to modulate the volume and the shape thus change the corresponding optical resonance wavelength. It causes severe change of optical response of metal nanoparticles and thus reflects onto the transient change of reflectivity and transmissivity of the probe that is located near the plasmon band.

Thanks to the abundant LSPR studies on 2D-periodical metal nanostructures [5.4], we know that the resonance of metal nanodisk array depends on size, geometry, periodicity, and permittivities of the metal and the environment. We suggested this is the reason that why we can see strong sensitivity on detection of vibration modes of Au nanodisk in infrared probe (1120nm), but it disappeared in that of 880nm probe. Also, it can explain why we see the abrupt change of signal as the rod become greater than ~300nm under the 1120nm probe since the plasmon resonant band would be redshifted

from the used probe (1120nm). The transmission and reflection spectra of the samples was preliminary examined to support the argument. The results exhibited that the transmission has a valley at around 1.1 μm for the sample of 273nm diameter, and the valley is blueshifted for the sample of small diameter (with the same period of 355nm). The character is corresponding to that of LSPR in metal nanodisks. However, the further investigation about the characters including the resonance field distribution in space and the width of the resonance band is beyond this thesis scope, so the discussion is left here.

5.2.3 Time Domain Analysis

Here, as we have proposed plasmon resonance would play an important role for infrared probe, we know that the gold nanodisk not only serves to be an opto-acoustic transducer but also a highly sensitive acoustic detector via the LSPR effect. For the excitation of NAWs, vibration of a nanodisk would relax by launching acoustic waves into the GaAs nanorod. Therefore the transducer can be viewed as a source that emits acoustic waves with specific frequency into the GaAs nanorod.

By testing a series of samples with different diameter, it is observed that although the frequencies are different, the appearing time of the echo are roughly the same, as shown in Fig. 5-6. (In fact, not all the samples of smaller diameter have clear echo signal; the echo is obscure in the cases of rod diameter small than 180nm owing to the lower SNR ratio.)

The similarity in echo time of the cases is a consequent result for the excitation comes from the lateral vibration, i.e. when the rod diameter becomes smaller, also as the attached Au nanodisk, the frequency of the lateral vibration thus become higher. It leads to the same crossing point on the dispersion curve, so excited acoustic wave packets are

with the same group velocity. The explanation is illustrated in Fig. 5-13.

Since the echo-like signals occur around 400ps~500ps, it means acoustic waves emitted were reflected and back to Au nanodisk thus being detected once again. According to the measured echo time which is less than 1 ns, there is no possibility to claim the waves are reflected at the bottom of the substrate because the substrate thickness is around 350 μm (a typical value for GaAs wafers). Therefore the only possibility should be the rod-substrate interface which forms a shape discontinuity and may interrupts the propagation of acoustic waves to cause an additional reflection. In the following section, the echo signal would be compared to the simulation by considering dispersive behavior and reflection at the rod-substrate interface of guide modes in a GaAs nanorod.

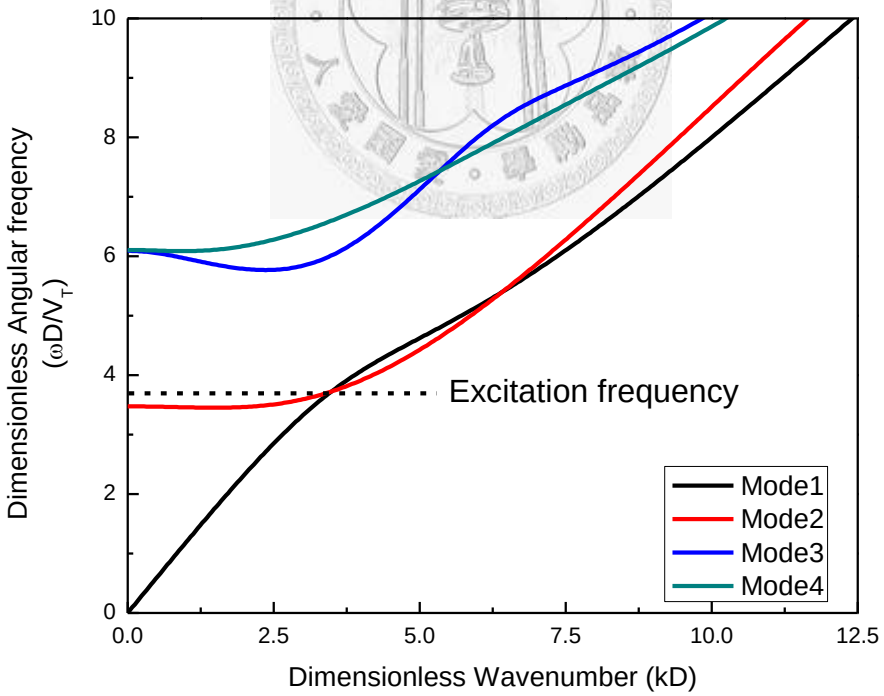

Fig. 5-13 Dimensionless dispersion relation of an acoustic cylindrical waveguide with infinite length (made of GaAs). The horizontal dashed line represents the dimensionless excitation induced by the lateral vibration of the Au nanodisk.

5.2.4 Group Velocity of Acoustic Wave Packet

These echo-like signals provide us information about propagation of the guided NAWs within the GaAs nanorod. As we have deduced that the only possibility to make the acoustic waves be reflected is the rod-substrate interface, we can reasonably estimate the velocity from the measured echo-time and from the known length of the rod. In a dispersive system, group velocity of an envelope would be different to phase velocity of each frequency component. So the velocity of the echo stated here is "group velocity" since the excitation is viewed as a wave packet consisting of broadband angular frequency components. The traveling behavior of this acoustic envelope is related to the group velocity $V_g = \frac{d\omega}{dk}$. If the roundtrip time can be estimated, then the group velocity is given by

$$V_g = \frac{2L}{t}. \tag{5.1}$$

The group velocity of the envelope was roughly estimated from the peak of the observed echo. The results shows the velocity is around 2700m/s, which is an lower value than the typical velocities of the longitudinal (4731m/s) and transverse wave (3347m/s). However, due to the strong dispersion, the envelope would be distorted when it propagate, thus makes it difficult to precisely determine the echo-time from the experimental data. Therefore, instead of analyzing from equation (5.1), we used initial oscillation signal to be an initial acoustic wave packet and decomposed it to every individual frequency phase component by performing FFT [5.7],

$$y_d = \int_{-\infty}^{\infty} Y(\omega) e^{-i\omega t} dt, \tag{5.2}$$

where y_d is the displacement, and $Y(\omega)$ is the amplitude of each component in angular frequency domain. The next step is let each component evolve according to the

dispersion relation obtained by the waveguide model which is a theoretical method we described in Chapter 3. Each angular component would experience different phase evolution, as the formula (5.3) states:

$$\Phi(\omega) = e^{(i\omega L/c(\omega))} \tag{5.3}$$

where $\Phi(\omega)$ is the phase shift of each angular component, L is the propagation distance, and $C(\omega)$ is the phase velocity derived from the dispersion relation ($C(\omega) = \frac{\omega}{k}$). After the evolution of each component, propagation of the envelope can be simulated by performing the inverse FFT to reconstruct it.

The dimensionless dispersion relation of GaAs nanorods is shown in Fig. 5-13. In the figure, it plots the central frequency of an excited envelope as the horizontal line. For the waveguide theory, the modes that could be excited are mode 1 and mode 2 for the frequency response. (Displacement field distribution of each mode are given in Fig. 5-14 and Fig. 5-15.) However, we excluded the possibility of excitation of mode 2 because the parity of displacement field conflicts to that of the excitation.

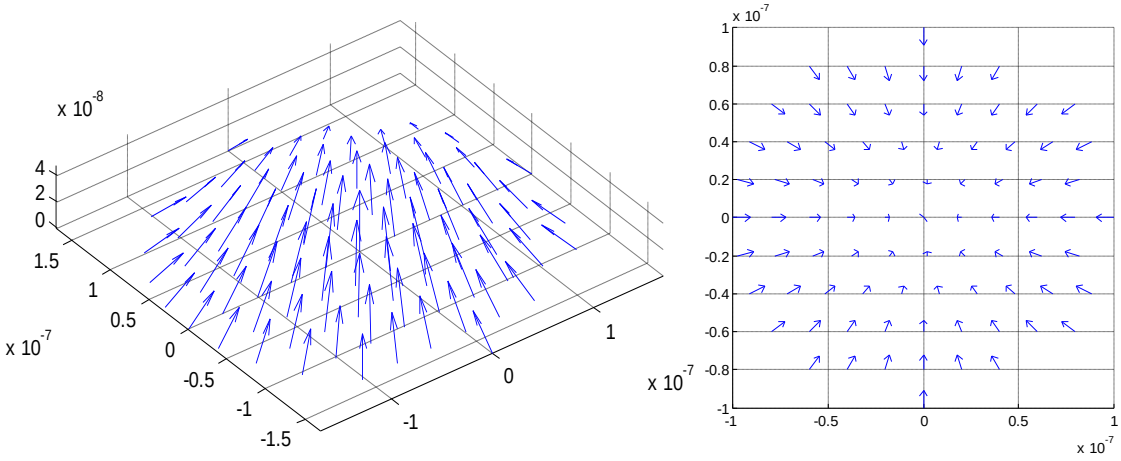

Fig. 5-14 Displacement field distribution of excited guided modes (Mode 1). (The pattern is drawn at the crossing points in the dispersion curve which is shown in Fig. 5-13.)

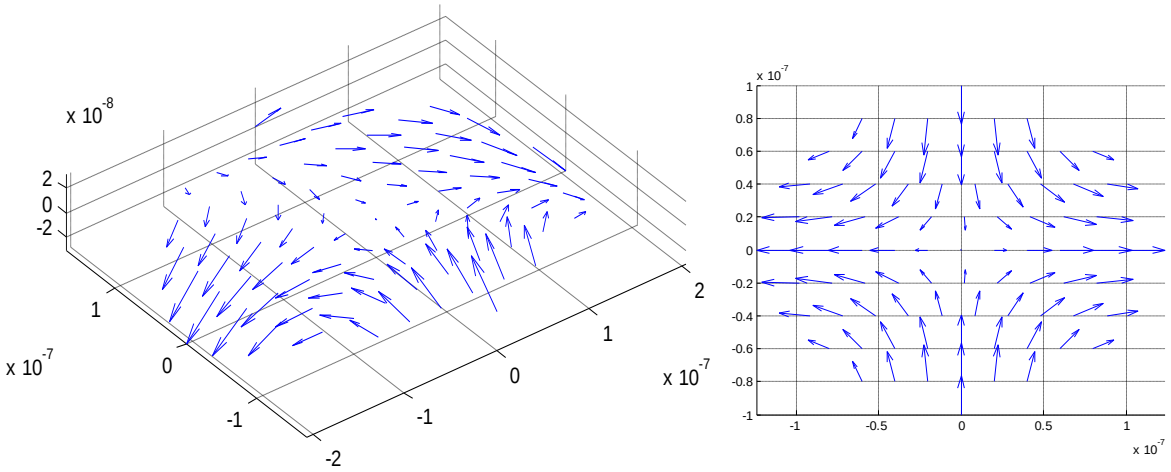

Fig. 5-15 Displacement field distribution of excited guided modes (Mode 1). (The pattern is drawn at the crossing points in the dispersion curve which is shown in Fig. 5-13.)

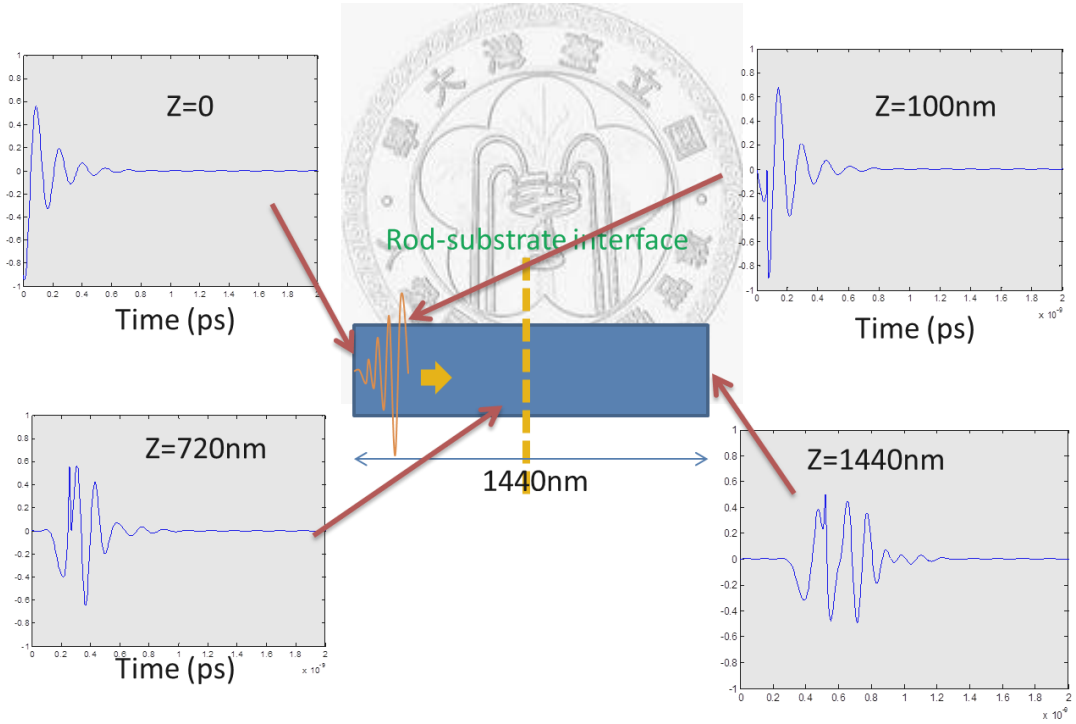

Fig. 5-16 Simulation of the excited wave packet propagation by considering the dispersive behavior of the fundamental guided mode (mode 1). (The simulation does not consider any loss.)

The simulation of mode 1 propagation is given in Fig. 5-16, in which we doubled the rod length to simulate the distance that acoustic waves travel through and did not consider any loss from propagation attenuation and partial reflection at the rod-substrate

interface. The graphs plotted the time response at different fixed spatial point. It is clear that the envelope would gradually depart from the original shape. Most importantly, as the simulation shows, the single roundtrip echo would be back at around 400~500ps, which is in good agreement with those observed in experiments.

Moreover, it is also reasonable to conclude that the residual oscillations after around 800ps are the echo (the second echo) that experienced double roundtrip inside the rod since the arrival time is coincidence to the twice as that of the first echo.

The simulation about the single and the double roundtrip echoes is shown in Fig. 5-17. (Although some of other data do not have obvious character to distinguish the second echo from the first one, it may be caused by the effects such as strength of bonding of deposited Au and SNR issue which make the oscillatory signal persist for longer time and thus mix with the second echo in time domain.)

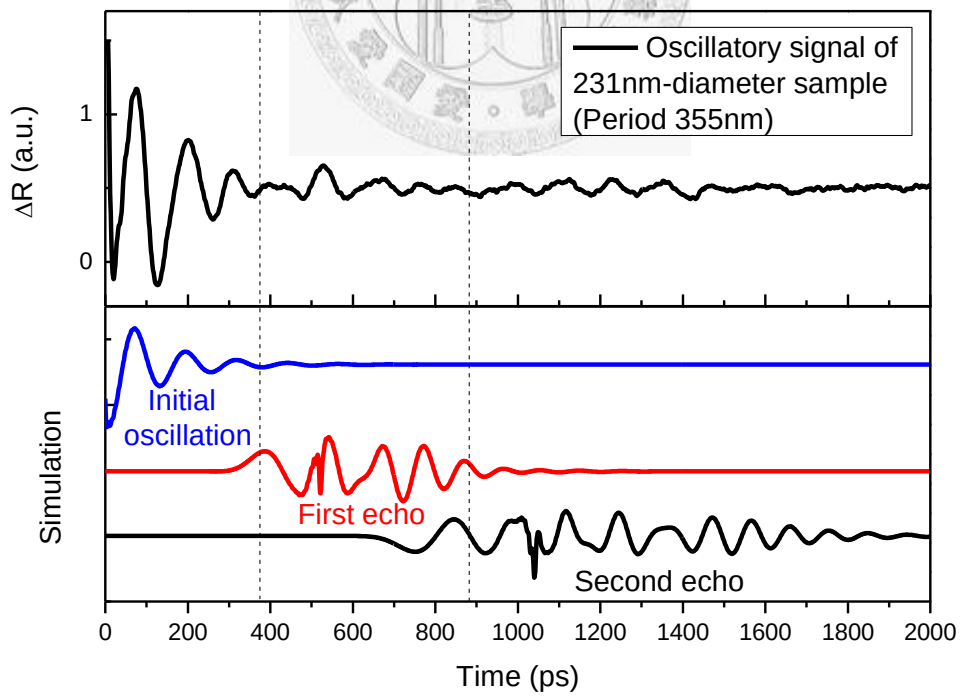

Fig. 5-17 Simulation of the single and the double roundtrip echo. (The simulation does not consider any loss for the echoes.)

Also, as we have claimed that excited propagating mode should be mode 1 only, no other propagating mode that possesses the same frequency but slower group velocity could exist in the GaAs NR. Therefore the echoes that experienced double roundtrip exists and contribute the signal we observed.

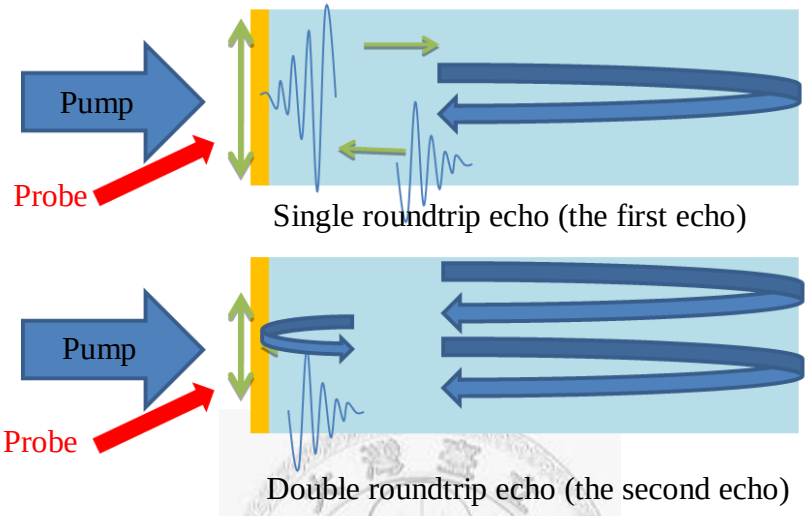

Fig. 5-18 Schematic diagram for the echoes observed in experiments

But one might suspect that could the acoustic waves of GHz be still alive after traveling such a long distance? The answer is probably yes, thanks to the reference [5.8], in which the author measured the attenuation of acoustic phonon of 56GHz inside a bulk GaAs crystal. The value they obtained is around 0.035 μm^{-1} at room temperature. If we use the value to test the propagation attenuation after propagating through 1.4 μm (the double rod length), we find only 5% loss to the waves.

Thus, we daringly ignored the attenuation since the excited frequency is one order less to that of reference [5.8] reported. Moreover, one would again suspect that surface roughness of the nanorod should make an additional loss as we compared to the bulk crystal. However, the roughness is around the order of 10nm, which are smaller than excited acoustic wavelength (~200nm), so we believe the attenuation is still less than the case of reference [5.8]. For the above reason, it is possible for availability to see the

echo of one-roundtrip and the echo of double-roundtrip in the nanorod. As for the echo of triple-roundtrip, it is unclear since the strength is smaller and the signal is mixed with the previous echo due to the spread waveform caused by the dispersion. Therefore, the third echo was left and without discussed here.

5.2.5 Roundtrip Loss Inside the GaAs Nanorod

By the aid of LSPR that enhances the detection sensitivity of acoustic modes in Au nanodisks, the signal that is different from the radial breathing mode of individual rod was observed. We thus decomposed the signal into three parts: initial oscillation which represents the initial vibration of the Au nanodisk, and the first and second echoes that represent the single and double roundtrip travel of coupled propagating modes that suffer dispersion and loss inside the GaAs nanorod. For a simplified 1D model, the loss includes the propagation attenuation and partial reflection at the bottom of the rod (rod-substrate interface).

Fig. shows the simulation of the echoes of single (the first echo) and double (the second echo) roundtrip that discussed in the previous section. As Fig. 5-17 shows, there are mixture of each part due to the spread caused by the dispersion. Therefore the amplitude comparison of each part by performing FFT would be unreasonable since the correct contraction of each part in the different timeframe is difficult.

The analysis of the ratio between the first and the second echo was conducted by fitting the experimental traces instead. As the same approach used in Section 5.2.4, the parameters of initial oscillations were obtained by fitting the exponential-decay cosine function. The echoes of single and double roundtrip were then simulated by setting the propagation distance equivalent to the double and the quadruple length of the rod. By means of adjusting a suitable strength of each echo and the rod length (the range was

adjusted in a range of 700nm to 750nm, which is acceptable tolerance of the identification from the SEM), the simulation was then compared to the experimental trace to obtain a reasonable ratio between the echoes.

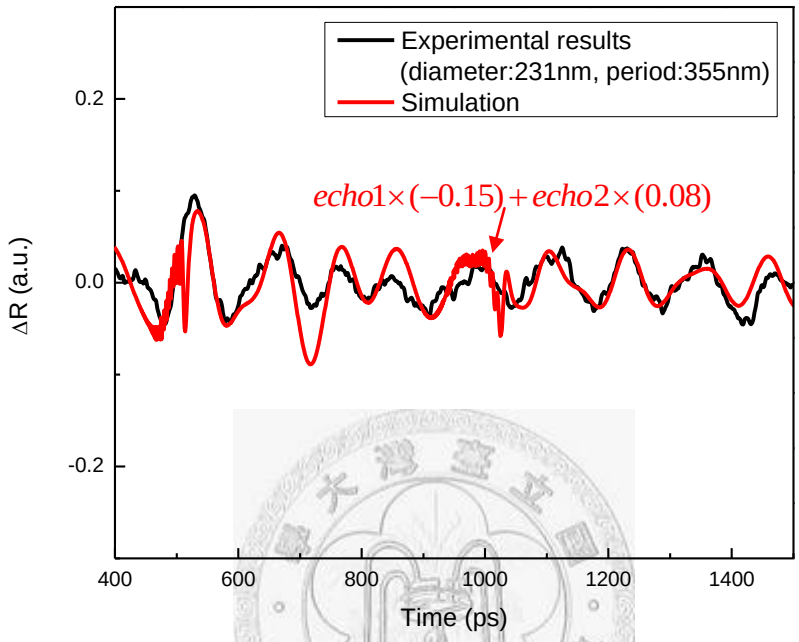

Fig. 5-19 Fitted result of the data. (Diameter:231nm, period 355nm)

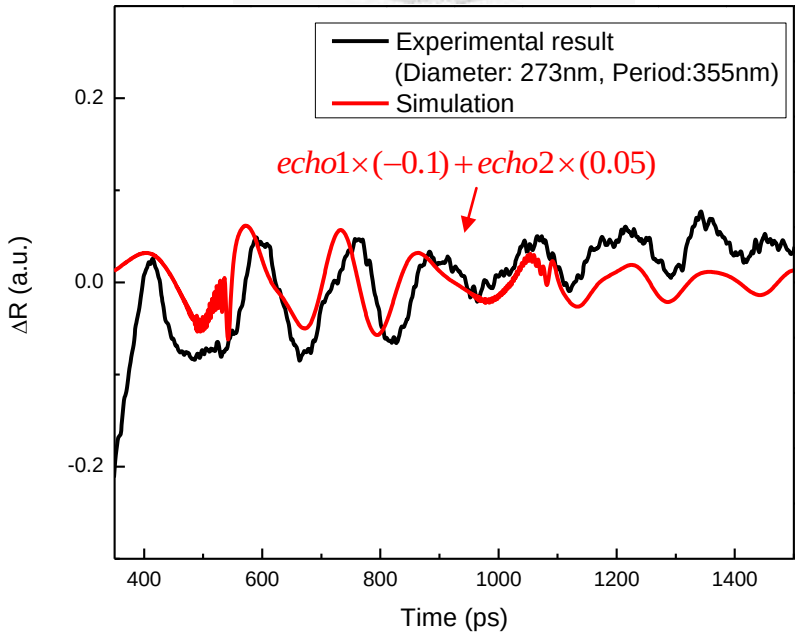

Fig. 5-20 Fitted result of the data. (Diameter:273nm, period 355nm)

Only two data were analyzed since the other have either a lower SNR or the severe mixture of each part (the mixture would be related to the damping character of the oscillation that would result from the bonding quality of the attached Au nanodisks and other imperfect defect of each sample) so that the characters are obscure.

Because we ignored the propagation attenuation, the ratio would give a value of the reflection coefficient at the rod-substrate interface for a simplified 1D propagation model [5.18] (a slight discrepancy from the reference is that the thickness of Au disk was ignored since it is much smaller than the wavelength of excited waves), as shown in equation (5.4):

$$\frac{echo2}{echo1} = r_{rob-substrate}. \tag{5.4}$$

The fitting result of the data of 231nm-diameter and of 273nm-diameter are given in Fig. 5-18 and Fig. 5-19, in which the ratios are given around -0.5 ± 0.2.

From the results, we found that although both of the rod and the substrate are made of GaAs, the transmission is not equal to 1 because of the mode matching, which has been demonstrated in some theoretical studies [5.12][5.13] (However, the studies are still limited to guided waves of low wavenumber). Most importantly, it is the first time of experimental attempt to measure the reflection coefficient of guided waves at abrupt junctions. In addition, the negative sign means the phase inverse of the reflected waves. The fact is reasonable since the end that attached to the substrate can be viewed as an rigid boundary to a certain degree for lateral modes.

Moreover, the estimated reflection coefficients of both results are nearly identical. Because the analyzed data are only two, the dependency on the diameter is not clear. However, we suggested in our cases the measured coefficients should be the same since the modes excited by the lateral vibration of the disks are effectively equivalent (the

same crossing point in the dispersion curve, as shown in Fig. 5-13.).

On the other hand, the ratio between the first echo and the initial oscillation is around 0.10~0.15, which is much lower than the ratio of the first and the second echo. We suggested that because of the formation of guided waves excited by the lateral vibration of the disk is related to the mode conversion due to the coupling between the resonant mode of the disk and propagating mode of the nanorod.

According to the waveguide theory, not all the excitation field would couple propagating modes. Actually, propagating modes are the solutions of an infinite waveguide. But as for a cylindrical rod with finite length, many researchers have pointed out those individual mode cannot simultaneously satisfy the boundary conditions of end surfaces. Therefore, they developed a “mode matching technique” to match the end conditions [5.9]. However, since the number of propagation modes at the certain frequency is finite, a set consisting of propagating modes merely could not form a complete basis to match the arbitrary end boundary [5.10].

The evanescent modes are the solution to this problem. J. Adam [5.11] has pointed out there are infinite complex solutions of wavenumber correspond to a specific frequency, and thus they do expand a complete set and can be used to solve the problem. Therefore based on the waveguide model, the excitation does not excite merely the fundamental propagating mode but also some other evanescent modes in our cases. However, only propagating modes would propagate and be reflected to form an echo. Therefore we suggested that a phenomenological coupling should contribute to the ratio between first echo and the initial oscillation. By assuming the formation of echo that experience two times of the mode conversion (couples out and couples back to the gold disk), the phenomenological coupling coefficient can be estimated as 0.3~0.4 (based on the analyzed data).

As for the oscillations of high frequency with around 50-60GHz which was induced from the thickness vibration, no clear echo signal related to this high frequency is observed experimentally, as shown in Fig.. shows the bandpass filtered (40-70GHz) result and the frequency spectrum of the range extended within 20-90GHz, in which the amplitude of the signal and the noise level are defined. (Only the data with the best SNR is shown below.)

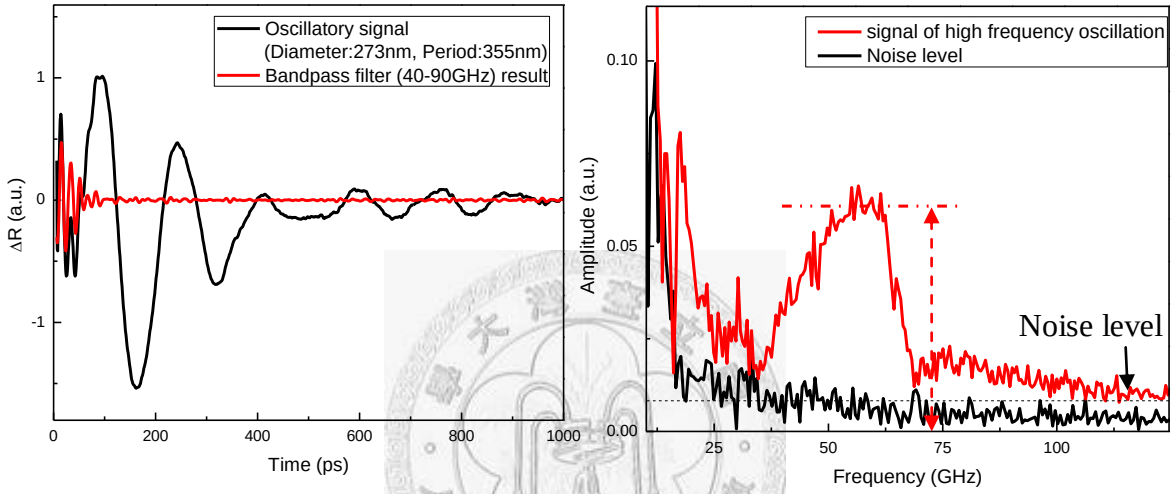

Fig. 5-21 (a) Background-removed oscillatory signal of 273nm-diameter sample (probe:1120nm). (b) Corresponding frequency spectra of the signal and the noise.

However, by assuming the noise level as the strength of the echo (if the strength is lower than the noise level, the echo is certainly obscure in the measured trace.), the echo would suffer a loss of 90%. By further assuming the loss is dominated by the propagation attenuation, the attenuation coefficient is estimated around $1.6\,\mu m^{-1}$, which is around fifty times larger than the value ($0.035\,\mu m^{-1}$) reported in reference [5.8]. The larger discrepancy reveals two possibilities: (1) the propagation attenuation of 50-60GHz phonons in a nanorod is much higher than that in a bulk, since the acoustic wavelength is in the same order as the roughness. (2) The propagating modes that is coupled by the thickness vibration of disk suffer better transmission at the rod-substrate

interface because of the mode matching. The concepts can be easily understood since the mode with a major displacement component in the axial are much easier to transmit into the substrate than the mode with a major component in the radial. The schematic diagram is shown in Fig. 5-22.

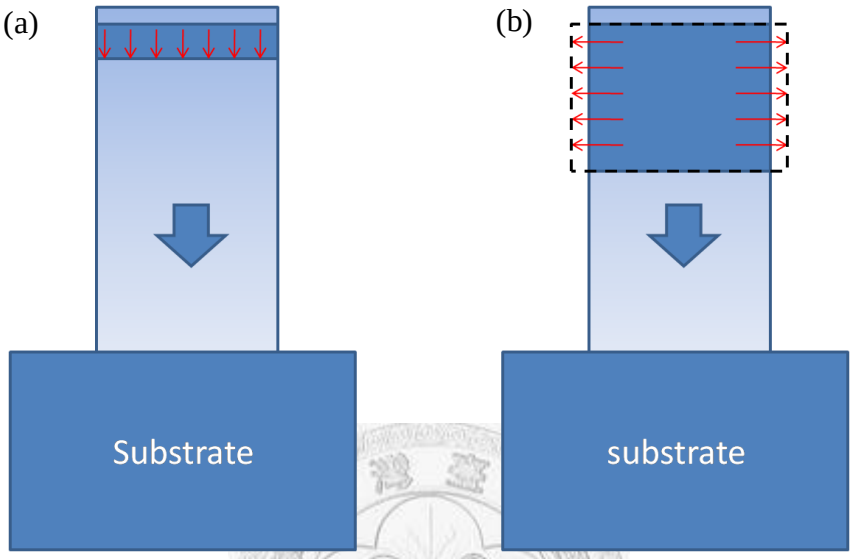

Fig. 5-22 Schematic diagram of (a) the mode with major component in axial direction and (b) the mode with major component in radial direction

5.2.6 Backward Brillouin Oscillation

Although experimental results of small-diameter (diameter < 300nm) cases for 1120nm probe had been explained and analyzed, the data of 340nm-diameter and 440nm-diameter are still left and without discussed. Since the optical probe wavelength (1120nm) is far from the resonance band of LSPs so that the signals of gold nanodisk vibrations are not clear in these cases. Contrarily, the dominating signal is attributed to the breathing mode of GaAs nanorods again. As shown in Fig. 5-23, the oscillatory signal of 440nm-diameter exhibits a pure damped oscillation character with the frequency of 6.9 ± 0.25 GHz (the predicted frequency of the breathing mode by formula (2.1) are around 7.2 GHz).

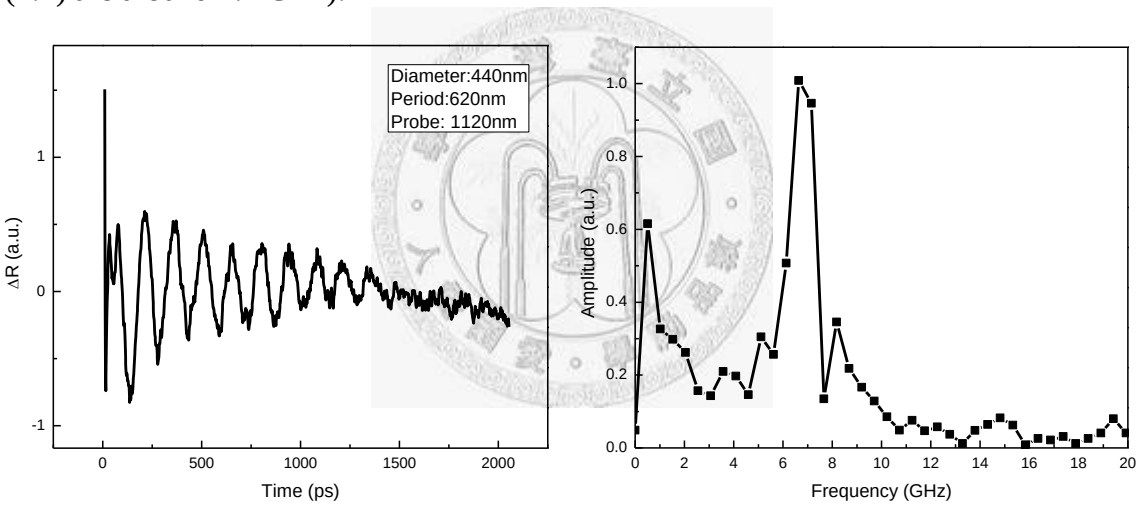

Fig. 5-23 Background-removed oscillatory signal of 440nm-diameter sample (probe:1120nm). (b) Corresponding frequency spectrum

However, the most interesting thing is the signal of 340nm-diameter, as shown in Fig. 5-24. The frequency spectrum show two significant peaks under 1120nm probe: one is 9.9 ± 0.25 GHz that is believed to be the breathing mode of GaAs nanorods because the frequency is roughly identical to those of 880nm probe case and the theoretical prediction. The other is 8.2GHz, however, it could not be identified as the signal of the vibration of nanodisks because the frequency is twice higher than the that of free lateral vibration of gold vibration (4.8GHz).

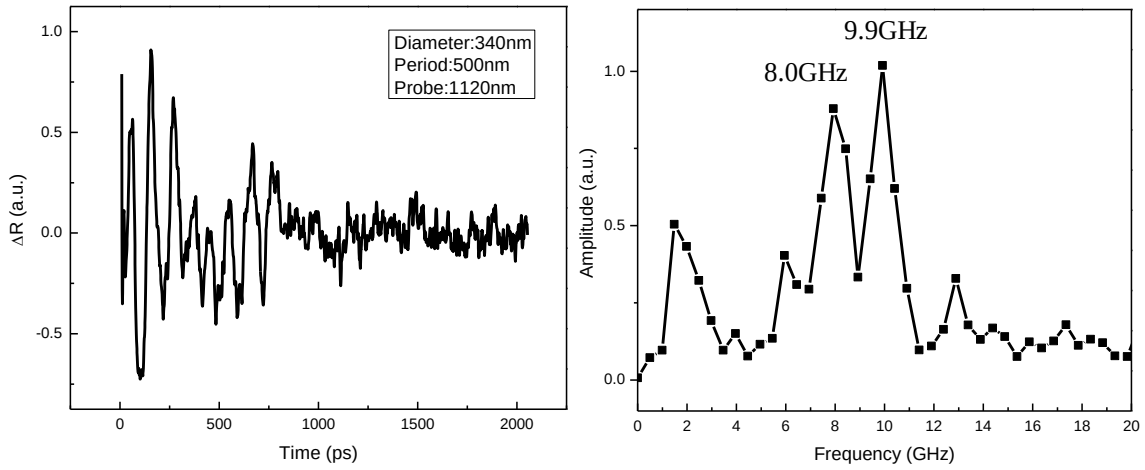

Fig. 5-24 (a) Background-removed oscillatory signal of 340nm-diameter sample. (b) Corresponding frequency spectrum. (Probe:1120nm)

But what does this signal could be? As we mentioned in Chapter 3, the left possible mechanisms include the SAWs and backward Brillouin oscillation. If SAWs is the answer, then we expect the signal should be observed in the identical sample under 880nm probe used but actually not. Therefore, for being the only candidate, backward Brillouin oscillation may be the way to explain the signal.

According to the mechanism, only the acoustic component which satisfies the phase matching condition (formula (2.3)) would contribute to Brillouin oscillation signals. As the equation stated, Brillouin oscillation frequency depends on optical refractive index of the sample and the phase velocity (dispersion relation) of acoustic waves. Owing to the fact that the size and spacing of the nanorod array are well below the optical wavelength of probe (1120nm), we treated the structure as an effective homogenous medium. By adopting Bruggeman theory [5.16][5.17], the effective refractive index could be calculated by solving the following equation:

$$f\frac{\varepsilon_{GaAs}-\varepsilon_{eff}}{\varepsilon_{GaAs}+2\varepsilon_{eff}}+(1-f)\frac{\varepsilon_{air}-\varepsilon_{eff}}{\varepsilon_{air}+2\varepsilon_{eff}}=0, \tag{5.5}$$

where ε_{GaAs}, ε_{air} ,and ε_{eff} are the dielectric constants of GaAs ,air, and the effective

medium, respectively. f is the volume fraction of GaAs nanorods. For the nanorod array of 340nm-diameter, 720nm-height, and 500nm-period, the volume fraction f is equal to 0.363, and n_{GaAs} is 3.45 at 1120nm ($\varepsilon_{GaAs} = n_{GaAs}^2$) [5.14]. Therefore, we obtained that ε_{eff} is 2.96 and thus the effective refractive index n_{eff} is 1.72. By the above calculated optical parameters, the acoustic component of fundamental guided mode that matches the condition of $k_a = 2k_{pr} = 1.93\times10^7$ (1/m) should contribute to the signal of backward Brillouin oscillation with 8.6GHz. This result is illustrated in Fig. 5-25.

The value agrees to the signal of 8.0 ± 0.25 GHz observed in the experiment. A slight discrepancy may result from the uncertainty of the dielectric constants of nanorods which may be different to those of the bulk crystal.

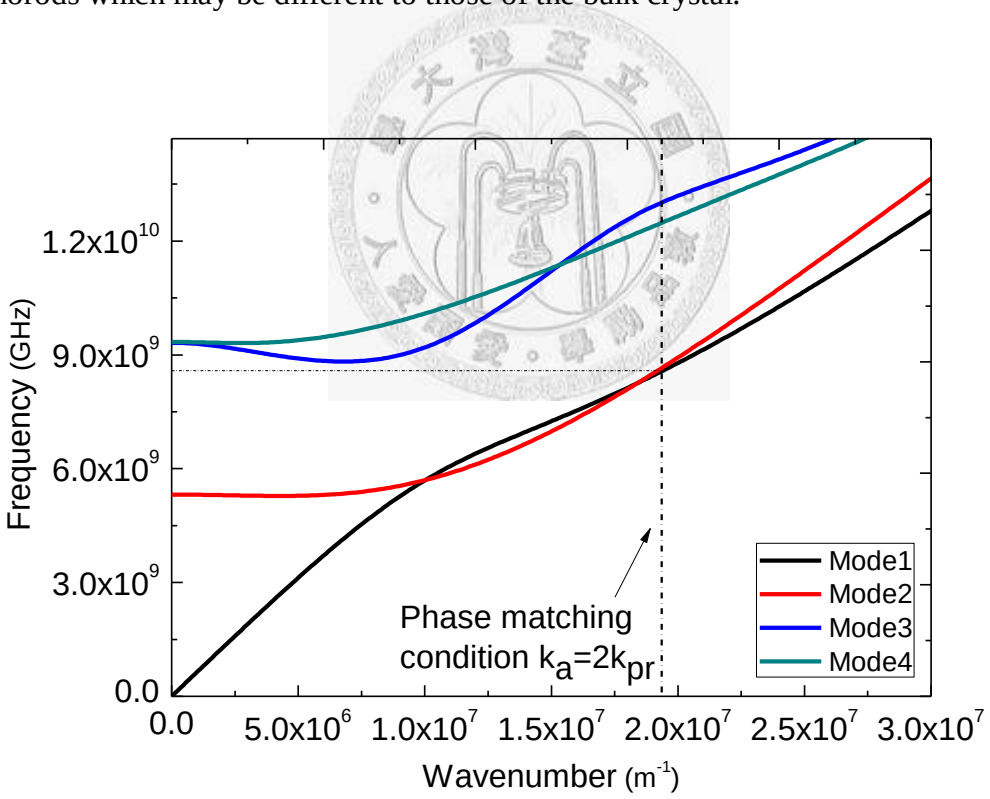

Fig. 5-25 Backward Brillouin oscillation induced by fundamental mode that satisfying the phase matching comditon

As we stated the signal of 8.0GHz is induced by the propagating guided mode via backward Brillouin oscillation, then the following problems come: why the signal disappears (or is not clear) in other cases?

To answer the question, we divided the cases into two groups: (1) for the case that with the intervention of LSPR, we suggested probe light cannot penetrate deeply into GaAs nanorods due to a strong absorption caused by the resonance of collective motion of electrons. No obvious backward Brillouin oscillation signals were observed because no interaction between the probe light and the guided modes in the nanorod region. These are the cases of small diameter (<300nm) under the infrared probe (1120nm).

(2) As for those without the resonance of LSPs, such as the cases of 440nm-diameter under 1120nm probe and 340nm-diameter under 880nm probe, one would expect the interaction occur. However, since the excited acoustic wave packet has limited frequency bandwidth, if the detected acoustic component is far away from the central frequency of the excitation, then no significant signal of Brillouin oscillation would be observed as well. The explanation was illustrated in the following figure.

In Fig. 5-26, dimensionless dispersion relation of guided mode was plotted for easier comparison between different cases. The gray region represents the limited bandwidth of excited acoustic envelope induced by the lateral vibration of the Au nanodisk. The horizontal dot line represents the central frequency, and the dot vertical line represents the phase matching condition for different cases. As it is shown in the figure, strength of the Brillouin oscillation signal would be much bigger for the case of 340nm-diameter under 1120nm probe since the detected component is much closer to the central frequency of excited waves.

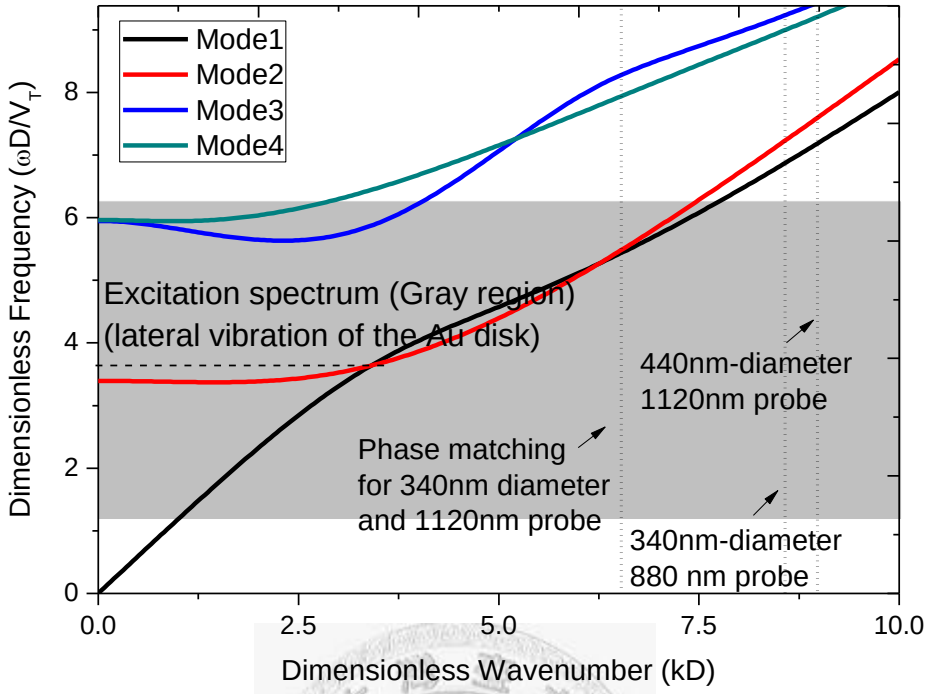

Fig. 5-26 Schematic diagram of explanation of the strength of the detected backward Brillouin oscillation signal

Reference

[5.1] G.V. Hartland, "Coherent vibrational motion in metal particles: Determination of the vibrational amplitude and excitation mechanism," *The Journal of Chemical Physics*, **116**, 8048, (2002).

[5.2] A. Devos, M. Foret, S. Ayrinhac, P. Emery, and B. Rufflé, "Hypersound damping in vitreous silica measured by picosecond acoustics," *Phys. Rev. B.* **77**, 100201 (2008)

[5.3] H. N Lin, H. J. Maris and L.B. Freund, K. Y. Lee, H. Luhn and D. P. Kern, "Study of vibration modes of gold nanostructures b picosecond ultrasonics," *J. Appl. Phys.* **73**, 37 (1993).

[5.4] Y. B. Zheng, B. K. Juluri, X. Mao, T. R. Walker, and T. J. Huang, "Systematic investigation of localized surface plasmon resonance of long-range ordered Au nanodisk arrays," *J. Appl. Phys*. **103**, 014308 (2008).

[5.5] P. Hanarp, M. Käll, and D. S. Sutherland, "Optical Properties of Short Range Ordered Arrays of Nanometer Gold Disks Prepared by Colloidal Lithography." *J. Phys. Chem. B.* **107**, 5768–5772 (2003).

[5.6] C. L. Haynes, A. D. McFarland, L. L. Zhao, R. P. Van Duyne, and G. C. Schatz. "Nanoparticle Optics: The Importance of Radiative Dipole Coupling in Two-Dimensional Nanoparticle Arrays." *J. Phys. Chem. B*. **107**, 7337–7342 (2003).

[5.7] A. D. Puckeet, M.L. Peterson, "A semi-analytical model for predicting multiple propagating axially symmetric modes in cylindrical waveguides," *Ultrasonic* **43**, 197 (2005).

[5.8] W. Chen, H. J. Maris, Z. R. Wasilewski, and S.-I. Tamura, " Attenuation and velocity of 56GHz longitudinal phonons in gallium arsenide from 50K to 300K." *Philosophical Magazine Part B*, **70**, 687-693 (1994).

[5.9] L. Kari. "Axially symmetric modes in finite cylinders—the wave guide solution." *Wave motion* **37**, 191-206, (2003).

[5.10] A. E. H. Love, *A Treatise on the Mathematical Theory of Elasticity*, 4th ed,. Cambridge University Press, Cambridge, 1927.

[5.11] J. Adem, "On the axially symmetric steady wave propagation in elastic circular rods." *Quat. Appl. Math.* **12**, 261-275 (1954).

[5.12] M.C. Cross and Ron Lifshitz, "Elastic wave transmission at an abrupt junction in a thin plate with application to heat transport and vibrations in mesoscopic systems," *Phys. Rev. B.*, **64**, 085324 (2001).

[5.13] R. Prasher, T. Tong, A. Majumdar, "An acoustic and dimensional mismatch model for thermal boundary conductance between a vertical mesoscopic nanowire/nanotube and a bulk substrate." *J. Appl. Phys.* **102**, 104312 (2007)

[5.14] D. T. F. Marple, "Refractive index of GaAs," *J. Appl. Phys.* **35**, 1241-1242 (1964).

[5.15] D. E. Aspnes, "Optical properties of thin films," *Thin Solid Films*, **89**, 249, (1982).

[5.16] G. A. Niklasson, C. G. Granqvist, and O. Hunderi, "Effective medium models for the optical properties of inhomogeneous materials." *Appl. Optics*, **20**, 26 (1981).

[5.17] H. Y. Chen, H. W. Lin, C. Y. Wu, W. C. Chen, J. S. Chen, and S. Gwo, "Gallium nitride nanorod arrays as low-refractive-index transparent media in the entire visible spectral region," *Opt. Express*, **16**, 8106, (2008).

[5.18] T.C. Zhu, H.J. Maris, and J. Tauc, "Attenuation of longitudinal-acoustic phonons in amorphous SiO2 at frequencies up to 440GHz," *Phys. Rev. B.*, **44**, 4281 (1991).

Chapter 6 Summary and Future Work

In summary of this thesis, ultrafast pump-probe studies of acoustic dynamic responses of Au-attached GaAs nanonod array and preliminary experimental investigations of guided NAWs in nanorod were carried out. To the best of our knowledge, the study of acoustic guided modes in the nanorod is the first time to be reported.

Unlike the other pump-probe studies on vibration mode of semiconductor and metal nanostructures by homogenous optical-illuminating excitation scheme, the Au nanodisk was designed to deposit on the top of GaAs nanorods to serve as a transducer that launches acoustic wave into the nanorod.

Although the samples was designed to study the acoustic guided modes confined to the nanorod, the excitation could excite other possible acoustic dynamics including the radial breathing mode of GaAs nanorod, surface acoustic modes in surface-patterend structures, backward Brillouin oscillations, and the vibration of the attached Au nanodisks in Au-attached GaAs nanorod array.

Experimental results show the detection of fundamental radial breathing mode of GaAs nanorods under 880nm probe used. However, as the probe wavelength was chosen from 880nm to 1120nm, the oscillatory signal alters to the vibration of Au nanodisks in the cases that the diameter is smaller than 300nm (period 355nm and 300nm). The intervention of resonance of LSP of Au nanodisks might be the key for the enhancement on detection sensitivity of acoustic modes in the Au nanodisk thus makes the signal change. Therefore, under this scheme, the gold nanodisk is not only an opto-elastic transducer but also a highly sensitive acoustic detector to detect the reflected waves. For these cases (diameter < 300nm and probe is 1120nm), the initial

vibration of gold nanodisk and echo signal were clearly observed. Arrival time of echo signal shows good agreement to the simulation of acoustic waveguide model based on the RUS method that considers anisotropic elastic properties of GaAs and assumes infinite rod length with free boundary. The fact reveals that the velocity of acoustic wave packets that propagates inside a nanorod is lower than the typical one of longitudinal and transverse waves in the bulk GaAs crystal ($V_T = 3347 m/s$ and $V_L = 4731 m/s$ in [001]).

Due to the reflection at rod-substrate interface, the first and the second echo were observed. Both echo and initial ringing signals were compared to quantitatively estimate the coupling (the coupling between vibration mode of Au nanodisk and guided mode of GaAs nanorod), and the reflection coefficient of guided waves at the rod-substrate interface.

This technique might provide a way to investigate the guided acoustic modes in nanorods that has not been studied yet, and it also gives an experimental measurement of reflection of guided waves at abrupt junctions. Based on the experimental results, we concluded the modes matching is an important issue for the transport between the nanorod and the substrate although both of them are made of the same material. The frequencies of NAWs investigated here are several GHz where the phonons served as the dominant heat carrier at 1-10K. The performed ultrasonic-based experiments thus provide another insight to the novel thermal transport properties at abruption junction of low-dimension nanostructures.

In addition, for the 340nm-diameter case that LSPR is far away from the probe wavelength (1120nm), backward Brillouin oscillation signal appears for the better overlap between the detection parts and limited excitation band in frequency domain.

The Brillouin oscillation signal is different to the echoes that detected by the gold nanodisk; it provides another information including the phase component of dispersion relation and the optical refractive index of sub-wavelength nanostructures.

Being the first stage of investigation of guided NAWs, the thesis made a start point to the further investigation on the waveguide utility of nanorods. Based on this work, the selection of excited modes could be possible by changing the transducer, and even possible to measure and depict the dispersion relation of anisotropic nanorods. In addition, the mode matching between different nanostructures studied could be further studied to aid the implementation of nano-acoustic waveguiding system in the future. The different properties of each mode could be even used for the future application in nano-acoustic devices for sensing and imaging.